Saturation Curve Analysis of Humidification-Dehumidification Desalination Systems and Analysis of Reversible Ejector Performance

by

Ronan Killian McGovern

BE (Mechanical Engineering), University College Dublin (2010)

Submitted to the Department of Mechanical Engineering
in partial fulfillment of the requirements for the degree of

Master of Science in Mechanical Engineering

at the

MASSACHUSETTS INSTITUTE OF TECHNOLOGY

February 2012

Author .....
Department of Mechanical Engineering
Jan 20, 2012

Certified by ....
John H. Lienhard V
Collins Professor of Mechanical Engineering
Thesis Supervisor

Accepted by .....
David E. Hardt
Chairman, Committee on Graduate Students

Saturation Curve Analysis of Humidification-Dehumidification Desalination Systems and Analysis of Reversible Ejector Performance

by

Ronan Killian McGovern

Submitted to the Department of Mechanical Engineering
on Jan 20, 2012, in partial fulfillment of the
requirements for the degree of
Master of Science in Mechanical Engineering

Abstract

The limitations upon the efficiency of humidification-dehumidification (HDH) desalination systems are investigated. Secondly, ejector technologies are analyzed as a means of powering desalination systems thermally. Thermal desalination systems offer advantages over membrane technologies in terms of robustness. They are less prone to scaling and fouling and capable of treating feed water of higher temperatures. One major drawback of thermal desalination is the high energy consumption, particularly for small scale systems. This work is motivated by the need for drastically improving the efficiency of thermal desalination technologies, particularily those on scales of 1 to 1000 m^3 per day.

Given multiple liquid and gas streams and simultaneous heat and mass transfer, the limits on the performance of HDH systems are not easily recognisable. By considering the saturation curve for moist air, a methodology is proposed to graphically understand these limits. A pinch point methodology is employed to evaluate the impact of heat and mass exchanger size upon performance. The impact of salinity upon the design methodology is described. As the pinch point temperature and concentration differences decrease, the gained output ratio (GOR) is shown to increase and recovery ratio is shown also to increase. There is shown to be a critical pinch point temperature difference beyond which there is no advantage to having multiple stages, each with different liquid to dry air mass flow ratios. Finally, the GOR is shown to increase as the temperature range of the cycle decreases.

Little attention is given in the literature to the definition of an ejector efficiency. Here, the entrainment ratio of real devices is compared to the reversible entrainment ratio and denoted the reversible entrainment ratio efficiency. The definition of different performance metrics for ejectors are analyzed and compared. Graphical illustrations are provided to support intuitive understanding of these metrics. The performance metrics are applied to existing experimental data. The behaviour of reversible ejectors is investigated. Analytical equations are also formulated for re-

versible ideal-gas ejectors. For general air-air and steam-steam ejectors, the exergetic efficiency η_X is found to be very close in numerical value to the reversible entrainment ratio efficiency, η_{RER}.

Thesis Supervisor: John H. Lienhard V
Title: Collins Professor of Mechanical Engineering

Acknowledgments

I would like to express my great appreciation for the support provided by the International Fulbright Science & Technology Award funded through the U.S. Department of State. I would like to thank the King Fahd University of Petroleum and Minerals for funding this research through the Center for Clean Water and Clean Energy at MIT and KFUPM.

Ba mhaith liom buíochas a gabhail do mo theaghlach, Jim, Stephanie, Aoife, Fergal agus an cailín a bhí chomh-lách liom ón lá gur shroich mé an tír seo, Ivonne. Táim anseo de bharr bhur tacaíochta. Beidh mé ar ais libh go mion minic. Go raibh míle maith agaibh.

THIS PAGE INTENTIONALLY LEFT BLANK

Contents

List of Figures

List of Tables

THIS PAGE INTENTIONALLY LEFT BLANK

Chapter 1

Introduction

Evaporation is one of the simplest ways one can conceive of a water purification system. Compared to membrane technologies such as reverse osmosis, thermally driven desalination technologies offer many advantages. Thermal systems are less prone to scaling and fouling and have the ability to deal with feed water of higher temperatures. A range of thermally driven desalination technologies is indicated in Fig. 1-1.

At the lower end of system scale in Fig. 1-1 lie solar stills, the simplest but most inefficient means of desalination. At the top end lie multi-effect distillation and multi-stage flash, systems that exist only at large scales and that exhibit higher efficiency. Between these two extremes lies a gap. To some extent, this gap is filled by energy efficient electrically driven technologies such as reverse osmosis (RO) or mechanical vapor compression (MVC). However, feed water of high salinity (beyond approximately 70 000 ppm) requires hydraulic pressures beyond what RO membranes can tolerate. The concentration of feed water achievable using mechanical vapor compression is also limited due to scaling concerns. RO is also unsuitable for high temperature feed water (beyond approximately 40° C) due to membrane deterioration. Furthermore, both RO and MVC cannot be driven by heat, without the provision of a heat engine. In remote environments with high levels of insolation, photovoltaic panels rather than solar heaters are required.

Returning to the gap in Fig. 1-1, we can ask whether this may be the place for

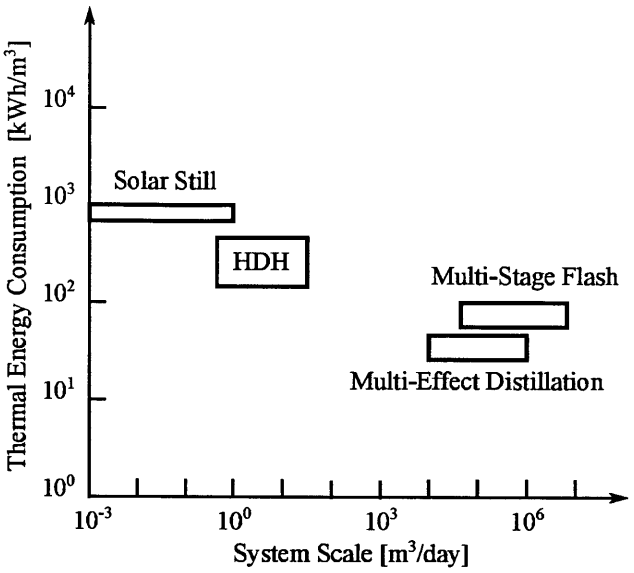

Figure 1-1: Thermal energy requirements versus scale of thermally driven desalination technologies

humidification-dehumidification (HDH) desalination, a technology almost as simple as a solar still but with the potential for higher efficiency. As it currently stands, it may be argued that low energy efficiency is the limiting factor in the deployment of HDH, particularly if the system is to be driven by solar power. With thermal energy requirements on the order of 100 kWh/m^3, the area and cost of solar collectors is prohibitive. Following this line of argument, for the HDH technology to progress, improvements in the energy efficiency of the system and the cost of providing that energy are required.

1.1 Understanding the Limits upon the Energy Efficiency of HDH

The HDH system, as outlined in Fig. 1-2 is not a simple one to analyze. These processes involve three distinct streams, feed water, moist carrier gas and condensate intercommunicating through simultaneous heat and mass transfer. Air enters the humidifier and is heated and humidified by a counterflow of hot water. The moist hot

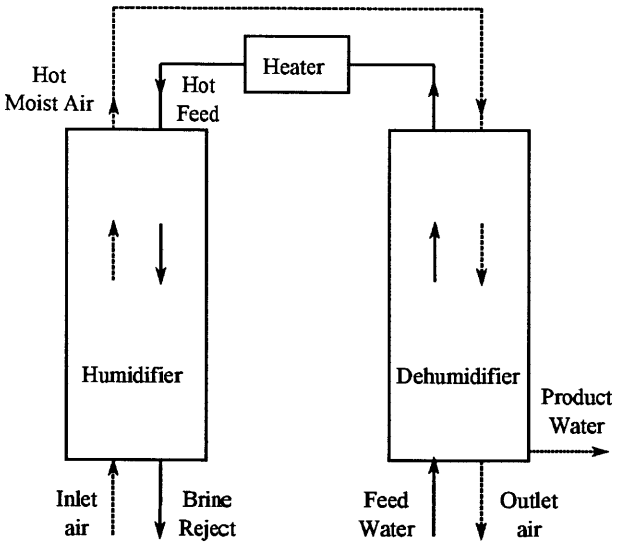

Figure 1-2: Humidification-dehumidification process

air is subsequently condensed in the dehumidifier as heat is transferred to the feed water. The pre-heated feed water at the outlet of the dehumidifier further increases in temperature in the water heater before being sprayed into the humidifier.

The optimal design of an HDH system requires the careful selection of the mass flow rate and temperature of each stream within the system. Given that the humidifier and the dehumidifier are intrinsically coupled, such optimal design requires an intuitive and complete understanding of the system's operation. Returning to Fig. 1-1, we can summarise the motivation for this research by posing the two following questions:

1. Why is the energy efficiency of HDH lower than other thermally driven technologies?

2. Through an improved understanding of the system and enhanced design methodologies, what are ultimately the limits upon energetic efficiency?

1.2 Characterizing Ejector Performance

Beyond the improvements in HDH system performance, sought in the Chapter 2 of this thesis, we can also consider means of reducing the cost of the thermal energy input to desalination systems. For example, at the simplest level, we could ask whether it is best to use solar energy for heating water or generating steam. Higher temperature solar collectors provide a higher exergetic input although their capital cost may be higher. For the same quantity of heat collected, the available work is greater. However, in the context of thermal desalination we must be vigilant about the risks of scaling at higher temperatures. We would like a heat source of high temperature but would like to maintain low brine temperatures. Using ejectors as a means of introducing a thermal energy input to a system is one solution to this apparent paradox.

An ejector, as indicated within Fig. 1-3, accelerates high pressure vapor to high velocity and low pressure. This low pressure provides a suction force that draws in a secondary fluid stream. After mixing, the fluid is decelerated in a diffuser and reaches the discharge pressure. Rather than solely providing a heating effect, an ejector allows flow work to be done on the entrained stream. Although the steam enters at high temperature, streams within the desalination system can be maintained at lower temperatures, thus avoiding the risks of scaling.

The role of the ejector in Fig. 1-3 is to provide a difference in pressure between the humidifier and dehumidifier, an idea that was initiated and developed by Narayan et al. [4, 5].

Beyond the application of Fig. 1-3, ejectors are widely employed in multi-effect-distillation desalination plants. Their use in vapor compression systems as a replacement for the mechanical compressor has also been suggested. In simple terms, an ejector serves as a mechanical compressor but at a much lower cost, due to its simple design with no moving parts. However, it is well known that the efficiency of ejectors is low, which limits their viability, particularly where solar collectors are concerned. Interestingly, when we posed the question as to how efficiency could be improved, we

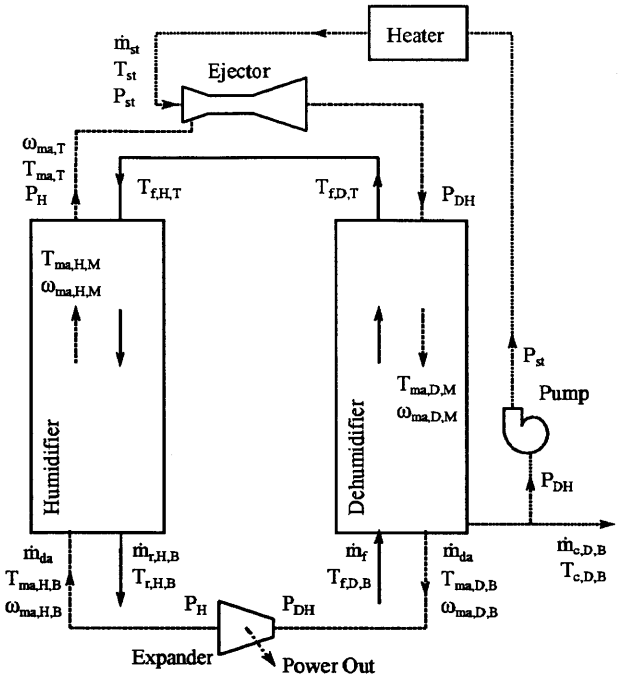

Figure 1-3: Ejector Driven HDH System

found that the definition itself of efficiency was not rigorously defined or investigated in literature. Before adopting an approach to improve ejector performance it became necessary to define appropriate performance parameters. These observations led to the two key questions motivating this ejector research.

1. How can a metric of ejector performance be defined by benchmarking real ejector processes against reversible processes?

2. How can the behaviour of a thermodynamically reversible ejector be described mathematically and graphically?

THIS PAGE INTENTIONALLY LEFT BLANK

Chapter 2

Evaluation of the Performance Limits of Humidification Dehumidification Desalination Systems via a Saturation Curve Analysis

Ronan K. McGovern, Gregory P. Thiel, Syed M. Zubair, John H. Lienhard V

Abstract

Due to the challenges involved in modelling combined heat and mass transfer processes, analyses of humidification dehumidification systems are typically experimental or numerical. Few provide an intuitive insight into the performance of HDH systems in terms of energetic efficiency (Gained Output Ratio - GOR) and recovery ratio. This chapter aims to bridge that gap. A methodology, revolving around the saturation curve of a moist carrier gas, is developed to analyze HDH systems. The problem of choosing optimal liquid and carrier gas mass flow rates within the system is reduced to a geometric problem involving graphs of enthalpy versus temperature. By employing a single extraction/injection of liquid from the humidifier to the dehumidfier the energetic performance is improved due to better matching between the saturation curve and the feed streams on an enthalpy-temperature diagram. The

GOR is shown to increase as the temperature range of the cycle decreases. A pinch point methodology is employed to evaluate the impact of heat and mass exchanger size upon performance. As the pinch point temperature and concentration differences decrease, the GOR is shown to increase and recovery ratio is shown also to increase. There is shown to be a critical pinch point temperature difference beyond which there is no advantage to having multiple stages, each with different liquid to dry air mass flow ratios. Finally, the impact of salinity upon the design methodology is described.

Nomenclature

Acronyms

HDH	Humdification-Dehumidification
GOR	Gained Output Ratio
PPTD	Pinch Point Temperature Difference
PCTD	Pinch Point Concentration Difference
RR	Recovery Ratio

Symbols

c	concentration [mol/m^3]
c_p	specific heat capacity at constant pressure [kJ/kg·K]
h	specific enthalpy [kJ/kg]
h_{fg}	latent heat of vaporization [kJ/kg]
H	enthalpy [kJ]
j	mass flux [kg/m^2·s]
$\dot{m}$	mass flow rate [kg/s]
M	molar mass [kg/kmol]
N	moles
p	partial pressure [bar or kPa]
P	absolute pressure [bar or kPa]
Q	heat input [kJ]
T	temperature [°C or K]
w	specific work [kJ/kg product]
Z	compressibility factor

Greek

Δ	change
ϕ	relative humidity [-]
χ	molar humidity [mol H_2O/mol carrier gas]
ω	humidity ratio [kg H_2O/kg carrier gas]

Subscripts

B	bottom
cg	carrier gas
da	dry air
D	dehumidifier
E	external
f	feed
H	humidifier
in	into system
l	liquid
ma	moist air
min	minimum
p	product
r	reject
T	top
v	vapor

Superscripts

~	molar
·	rate [s^{-1}]
*	per unit dry carrier gas

2.1 Motivation

Humidification-dehumidification (HDH) systems are commonly viewed as robust liquid purification systems, driven by heat and capable of operating on a small scale decentralized basis. Energy consumption is high compared to membrane based reverse osmosis technologies [6] but the components are simple and require low maintenance. In desalination applications, HDH systems purify saline feed water. From another perspective, the role of HDH systems could be to concentrate industrial waste water streams.

The premise underlying HDH is that by humidifying air (or another suitable gas) through the evaporation of a pure substance from a feed solution and its subsequent condensation, pure water vapor may be separated from its solutes and suspended solids. Subsequently, in the dehumidification process, the vapor is condensed to form a purified liquid product. The HDH system, Fig. 2-1, which separates the humidification and dehumidification processes, is one means of implementing a carrier gas based liquid purification process. This is in contrast to dewvaporation systems, where heat is transfered from the dehumidifier to the humidifier via a common heat transfer wall, [7].

The system described in Fig. 2-1 is a water heated open air HDH process. Air enters the humidifier from the surroundings and is heated and humidified by a counterflow of feed. The moist air then flows to the dehumidifier, in which the air is cooled and water vapor is condensed by a counterflow of liquid feed. The feed is heated in the dehumidifier and in the heater before being cooled and partially evaporated in the humidifier. The feed remaining at the bottom of the humidifier, known as the reject, exits the system. Crucial to the energy efficiency of carrier gas based liquid purification processes is the recovery of heat during air cooling and dehumidification for use during air humidification and heating.

Although HDH systems are potentially simple in terms of design and operation, their poor energy efficiency is a significant drawback. Some of the best systems still require 150 kWh of thermal energy per m^3 product water [8]. This inefficiency

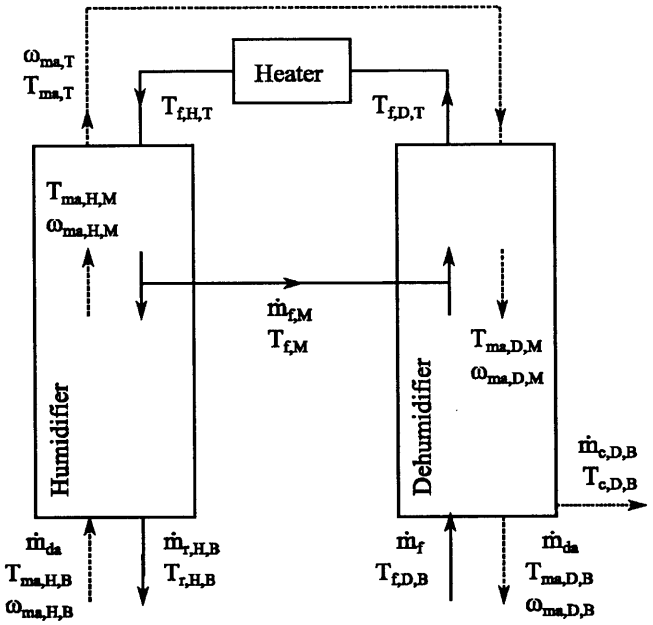

Figure 2-1: Water heated, open air, humidification dehumidification desalination system

has led to to numerous analytical, numerical and especially experimental studies [9]. The prevalance of experimental studies is somewhat of a testament to the difficulties involved in analyzing a system with three fluid streams (feed, condensate and carrier gas) undergoing simultaneous heat and mass transfer. At least two approaches to the analytical modelling of HDH have been taken. The first, employed by Narayan *et al.* [10], involves the use of an enthalpy based effectiveness to quantify humidifier and dehumidifier performance in a parametric study of HDH systems. Narayan *et al.* consider the thermal energy requirements for fixed component effectivenesses and cycle temperature range. By achieving a heat capacity rate ratio (liquid to moist air stream) of unity in the dehumidifier, the entropy generation per unit water produced in the system is minimized. In papers by Hou *et al.* [11], Hou [12] and Zamen *et al.* [13], the performance of the humidifier and dehumidifier is parametrized by specifying pinch point temperature differences. A key idea in this work is that the process path of moist air is considered to follow the saturation curve. Hou *et al.* [11] demonstrate that the thermal energy recovery rates increase rapidly as the temperature differences at the pinch points within the system decrease. Hou [12]

later explains that, by having a two stage cycle and therefore reducing the relative mass flow of air to water in the top of the cycle, the curvature of the saturation curve can be reduced. Thus, temperature differences between streams at the inlet and exit of the dehumidifer can be reduced. Zamen *et al.* [13] further build upon the work of Chou and describe a multi-stage HDH cycle within which the mass flow of air is reduced within each stage of higher temperature. This further flattens the saturation curve. The thermal energy requirements of the cycle are shown to decrease with an increasing number of stages.

Given this overview of analytical studies, we can list some of the key remaining questions:

1. How does the choice of the cycle temperature range affect thermal energy requirements?

2. How does the improvement achieved by implementing a multi-stage system relate to component sizes (*e.g.* pinch point temperature difference)?

3. What are the limits upon the fraction of feed water recoverable as product?

4. How does feed salinity affect the thermal energy requirements of HDH desalination?

The goal of this chapter is to address each of these questions in an intuitive manner, building upon and unifying results found in literature. Specifically, this chapter will describe a method of analysis, involving the saturation curve of a moist carrier gas, to provide a graphical insight into the design of HDH systems. In Section 2.2, the performance metrics for HDH systems are outlined. In Section 2.3, the saturation curves for a moist carrier gas and their relevance to the analysis of HDH are outlined. The saturation curve methodology is applied in Section 2.4. Finally, in Sections 2.5 and 2.6, the answers to the motivating questions above are provided.

2.2 Performance Metrics

Before proceeding with our discussion of approximations, we define key performance parameters for the HDH process. The first parameter of interest concerns the energetic performance of the system, measured by considering the mass (or moles) of water produced per unit of heat input to the cycle. Since this quantity is dimensional, it is common to multiply by the latent heat of vaporisation to obtain the Gained Output Ratio, or the GOR, a dimensionless quantity.

$$\mathrm{GOR} = \frac{\dot{m}_\mathrm{p} h_\mathrm{fg}}{\dot{Q}} = \frac{\dot{N}_\mathrm{p} \tilde{h}_\mathrm{fg}}{\dot{Q}} \tag{2.1}$$

The GOR is a measure of the latent heat of water produced per unit of heat input. There is no consensus in the literature upon the temperature at which the latent heat of vaporization should be computed. However, the current authors would suggest that it be evaluated at ambient temperature. In this way, we can envision a system that evaporates water at ambient temperature by operating at reduced pressure and subsequently condensing the water vapor without recovery of the heat of condensation. Such a system would have a GOR of 1.

Many HDH systems operate with a constant mass (or molar) flow rate of carrier gas. It is therefore useful to define all quantities on a carrier gas basis, *i.e.* per unit mass of carrier gas or per mole of carrier gas. Employing an asterisk to identify quantities measured on a carrier gas basis, the following expression for GOR is obtained:

$$\mathrm{GOR} = \frac{\Delta\omega h_\mathrm{fg}}{\dot{Q}^*} = \frac{\Delta\chi h_\mathrm{fg}}{\dot{\tilde{Q}}^*} \tag{2.2}$$

Then for a water heated system we have:

$$\mathrm{GOR} = \frac{\Delta\omega h_\mathrm{fg}}{\Delta h_f^*} = \frac{\Delta\chi \tilde{h}_\mathrm{fg}}{\Delta \tilde{h}_f^*} \tag{2.3}$$

The second measure of interest concerns the fraction of feed water that the system is capable of recovering as product. The recovery ratio captures this fraction and is

defined as the ratio of product water to feed water, either on a mass or molar basis:

$$\mathrm{RR} = \frac{\dot{m}_{\mathrm{p}}}{\dot{m}_{\mathrm{f,H_2O}}} = \frac{\dot{N}_{\mathrm{p}}}{\dot{N}_{\mathrm{f,H_2O}}} \tag{2.4}$$

The final measure of performance is the exergetic efficiency. This performance metric allows us to determine how close system performance is to being thermodynamically reversible. The exergetic efficiency is defined as the useful exergetic output of the system divided by the exergetic input. A detailed discussion of this efficiency for desalination processes is provided by Mistry *et al.* [6]:

$$\eta_{II} = \frac{\dot{X}_{\mathrm{out}}}{\dot{X}_{\mathrm{in}}} = \frac{\dot{m}_{\mathrm{p}} w_{\mathrm{min}}}{\dot{Q}^{*}\left(1 - \frac{T_0}{T_{\mathrm{in}}}\right)} \tag{2.5}$$

w_{min} refers to to the minimum work required to extract one unit of pure water from an infinite body of seawater. For seawater with a salinity of 35,000 ppm, the minimum work (calculated with feed and product streams at 25°)C is 2.71 kJ/kg pure water produced. For a water heated HDH cycle, the exergetic input to the system is in the form of heat transfer to the feed. T_{in} is the temperature at which heat enters the control volume of the HDH system. This temperature is somewhat ambiguous. Strictly speaking, if the feed is heated from 65°C to 70°C, for example, heat would enter the system over a range of temperatures. However, since the temperature range within the heater is small, heat will be considered to enter at a constant temperature, equal to the top temperature of the feed in the cycle. For an HDH cycle, it is convenient to write Eq. (2.5) in terms of GOR:

$$\eta_{II} = \frac{GOR \cdot w_{\mathrm{min}}}{h_{fg}\left(1 - \frac{T_0}{T_i n}\right)} \tag{2.6}$$

Of course, if analyzing an HDH system with pure water as the feed stream, the system provides no useful exergetic output, since pure water is produced from a feed of pure water. The exergetic efficiency is not of relevance in analyzing such a process. In other words, the second law efficiency only becomes useful when there is a useful exergetic output, *i.e.* when a saline feed stream is being purified.

2.3 Mass Balances, Enthalpy Balances and Saturation Curves

Saturation curves are extremely useful in visualising mass flows and energy flows within HDH. A plot of humidity ratio versus temperature allows us to visualise mass transfer, whilst a plot of enthalpy versus temperature illustrates energy transfer. These two plots share a common trait, in that their y-axes (humidity ratio and specific enthalpy) are both defined on a unit mass basis. This is possible since the mass flow rate of air through the system is constant. In this section, we describe how the conservation of mass and energy within humidifiers and dehumidifiers can be graphically represented. We also describe the influence of salinity upon the saturation curves.

2.3.1 Mass Balance and the Saturation Curve

In Fig. 2-2, we consider a general control volume for humidification or dehumidification. A stream of liquid and a stream of moist air enter and exit the control volume. Individual control volumes are also indicated for the gas mixture and the liquid. A portion of each individual control volume passes just inside the liquid on the liquid side of the gas-vapor interface.

When the mass flow of air is constant throughout the system, we may specify all other mass flow rates and state variables on a unit dry air basis. Conducting a vapor mass balance upon the overall control volume and the individual control volumes yields the following relations:

$$d\dot{m}_{\mathrm{l}} = -\dot{m}_{\mathrm{a}} d\omega = j_{\mathrm{v}} dA \tag{2.7}$$

For dehumidification, Eq. (2.7) describes the relation between the condensate production and the change in humidity ratio of the air. For humidification, Eq. (2.7) relates the mass of feed evaporated to the change in humidity ratio of the air. To quantify the rate of condensation or the rate of evaporation as a function of air temperature

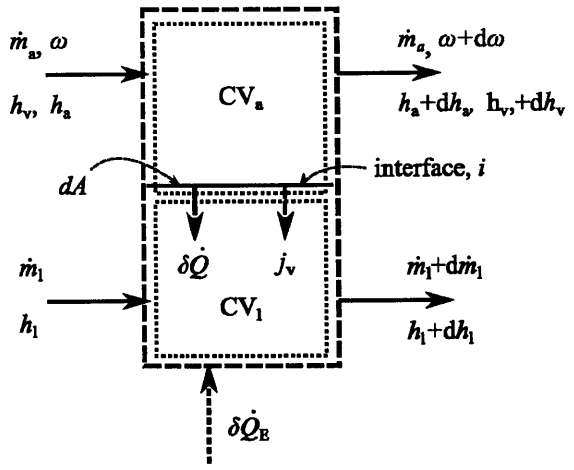

Figure 2-2: Control volume for a general humidification or dehumidification process

we can consider a graph of the saturated humidity ratio versus temperature. Two saturation curves for an ideal carrier gas are provided in Fig. 2-3. They correspond to a saturated ideal carrier gas in equilibrium with pure water and in equilibrium with seawater (at a salinity of 35 000 ppm). The properties moist air mixture in equilibrium with pure water are evaluated using the formulations presented by Hyland and Wexler [14]. The moist air mixture in equilibrium with seawater is approximated as an ideal mixture in calculating its properties and the saturation pressure of seawater is computed using correlations developed by Sharqawy *et al.* [15].

If the carrier gas is ideal, then the saturation curve on a molar basis is independent of the choice of carrier gas. Commonly in psychrometric charts the humidity is displayed on a mass basis, in which case Fig. 2-3 would be scaled by the molar mass ratio of the carrier gas. The ability of the ideal carrier gas to hold vapor increases rapidly with temperature due to the exponential dependence of vapor pressure on saturation temperature.

During dehumidification of a carrier gas-vapor mixture, the relevant saturation curve will always be that which is in equilibrium with pure water. During humidification, salinity will influence the vapor pressure and thus the saturation humidity ratio of the carrier gas. The difference in value of the saturation humidity ratio between

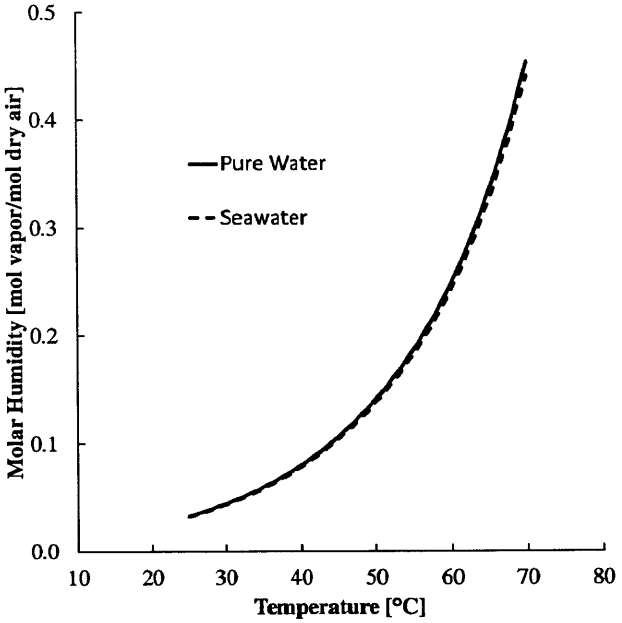

Figure 2-3: Molar ratio of vapor to carrier gas versus saturation temperature

seawater and pure water systems is approximately -8% at 25°C and -4% at 70°C.

2.3.2 Energy Balance and the Saturation Curve

Returning to Fig. 2-2, and applying the First Law to the control volume of carrier gas, we may relate the heat transfer rate to the specific enthalpies and mass flow rates:

$$-\delta\dot{Q} = \dot{m}_{\mathrm{a}}(dh_{\mathrm{a}} + \omega dh_{\mathrm{v}}) + \dot{m}_{\mathrm{a}}h_{\mathrm{v}}d\omega + j_{\mathrm{v}}h_{\mathrm{l,i}}dA \tag{2.8}$$

Employing Eq. (2.7), we substitute for j_{v}.

$$-\delta\dot{Q} = \dot{m}_{\mathrm{a}}\overbrace{[dh_{\mathrm{a}} + \omega dh_{\mathrm{v}} + (h_{\mathrm{v}} - h_{\mathrm{l,i}})d\omega]}^{dh_{\mathrm{a}}^{*}} \tag{2.9}$$

$\delta\dot{Q}_{\mathrm{E}}$ refers to an external heat transfer to the liquid stream. In an externally adiabatic humidifier this heat transfer would be zero. In a dehumidifier $\dot{Q}_{\mathrm{E}}$ would be negative and would represent heat transfer to a coolant. Applying the First Law to the liquid

control volume yields:

$$\delta\dot{Q}_{\mathrm{E}} + \delta\dot{Q} = \dot{m}_{\mathrm{l}} dh_{\mathrm{l}} + h_{\mathrm{l}} d\dot{m}_{\mathrm{l}} - j_{\mathrm{v}} h_{\mathrm{l,i}} dA \tag{2.10}$$

$$\delta\dot{Q}_{\mathrm{E}} + \delta\dot{Q} = \overbrace{\frac{\dot{m}_{\mathrm{l}}}{\dot{m}_{\mathrm{a}}} dh_{\mathrm{l}} + \frac{d\dot{m}_{\mathrm{l}}}{\dot{m}_{\mathrm{a}}}(h_{\mathrm{l}} - h_{\mathrm{l,i}})}^{h_{\mathrm{f}}^*/h_{\mathrm{c}}^*} \tag{2.11}$$

The above equations give rise to the definition of specific enthalpy on a dry air basis, denoted by h^*, to be used in all further analyses. For dehumidification, h_{c}^* would represent the specific enthalpy of the condensate on a dry air basis. In the case of humidification, h_{f}^* would represent the specific enthalpy of the feed on a dry air basis. Eq. (2.10) indicates that the process paths of liquid streams can be easily visualised on a diagram of h^* versus T. In the humidifier the evaporation rate is small compared to the mass flow of liquid. Liquid lines appear straight if drawn on Fig. 2-4 since $c_{p,\mathrm{l}}$ is almost constant with temperature. The slope of such a line will be dictated by the mass flow ratio (or the molar flow ratio) of liquid to dry air. In Fig. 2-4 the enthalpy per mole of dry air, h_{a}^*, is plotted versus the saturation temperature, for the cases where moist air is in equilibrium with pure water and with seawater (at 35 000 ppm).

Again, during dehumidification of a carrier gas-vapor mixture, the relevant saturation curve will always be that which is in equilibrium with water. During humidification, salinity will influence the vapor pressure and thus the saturation specific enthalpy of the moist air. The difference in value of the specific enthalpy of moist air between seawater and pure water systems is approximately -2% at 25°C and -3% at 70°C.

We would like to obtain an expression describing the shape of the saturation curve (equilibrium with pure water) in Fig. 2-4. Returning to Eq. (2.9), we can consider the order of magnitudes of each of the terms in dh_{a}^*,. We begin by considering $h_{\mathrm{v}} - h_{\mathrm{l,i}}$.

$$h_{\mathrm{v}} - h_{\mathrm{l,i}} \approx c_{\mathrm{p,v}}\left[T_{\mathrm{v}} - T_{\mathrm{sat}}(P_{\mathrm{v}})\right] + h_{\mathrm{fg}}(P_{\mathrm{v}}) + c_{\mathrm{p,l}}\left[T_{\mathrm{sat}}(P_{\mathrm{v}}) - T_{\mathrm{l,i}}\right] \tag{2.12}$$

$$\approx h_{\mathrm{fg}}(P_{\mathrm{v}}) \tag{2.13}$$

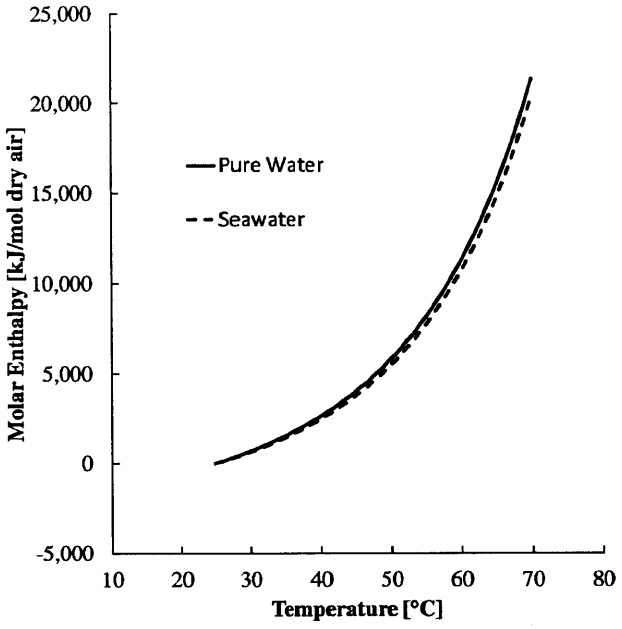

Figure 2-4: Saturation curve on an enthalpy-temperature diagram for a moist carrier gas on an enthalpy versus temperature diagram

The air and the vapor are at the same temperature, T_a, and the temperature difference between the liquid and the air would typically be below 10 °C. Consequently, h_{fg} dominates Eq. (2.12). We now introduce this approximation into Eq. (2.9) to obtain Eq. (2.14)

$$dh_a^* \approx \dot{m}_a \left(c_{p,a} + \omega c_{p,v} + h_{fg} \frac{d\omega}{dT_a} \right) dT_a \tag{2.14}$$

$$dh_a^* \approx \dot{m}_a h_{fg} d\omega \tag{2.15}$$

The humidity ratio of saturated air at 50°C is approximately 0.1 kg vap/kg air, while the slope of the saturation curve $d\omega/dT_a$ is approximately 0.005. At moderate and high temperatures (approximately 40 to 100°C) the value of dh_a^* is primarily dictated by the third term in (2.14). Hence, the shape of the saturation curve on a humidity-temperature and an enthalpy-temperature diagram are very similar in this region. This assertion will prove useful when evaluating the performance of HDH cycles in Sect. 2.5.

2.4 Application of the Saturation Curve Method

2.4.1 Modelling Approximations

The following four approximations are employed within our analysis:

1. Constant Pressure
2. Ideal Gas Behavior
3. Zero Salinity Feed
4. Saturation Curve Process Path

We now deal with each of these in turn.

Constant Pressure Approximation

Embodiments of the HDH cycle do exist within which the pressure of the gas mixture is varied in order to drive humidification and dehumidification, [4, 5]. In this work, only systems in which the pressure is approximately constant throughout are considered. Of course, a pressure gradient must be provided by a fan to circulate the carrier gas. Typically the pressure rise provided by fan would be expected to be on the order of a few kPa, compared to an absolute pressure of 100 kPa. Whilst this requires work input to the system, this work is small compared to the heat input to the system.

Ideal Gas Approximation

For HVAC analyses, the ideal gas approximation is very well accepted when modelling moist air mixtures. Sincee HDH systems operate over a higher range of temperature, and may be designed employing gases other than air, it is worth verifying the accuracy of ideal gas approximations. HDH systems operate at temperatures between approximately 20°C and 80°C and at pressures of 1 bar or lower, [16]. The ideality of gases may be verified by considering the compressibility factor at typical pressures

and temperatures of HDH systems. A compressibility factor close to unity indicates an ideal gas:

$$Z = \frac{Pv}{RT} \tag{2.16}$$

Calculation of this compressibility factor for helium, air, carbon dioxide and vapor indicates that, for the range of temperatures and partial pressures experienced in HDH systems, the compressibility factor is always between 0.99 and 1. For example, the compressibility factor of water vapor, helium, air and carbon dioxide in saturated vapor-carrier gas mixtures in thermal equilibrium with pure water at 50°C are 0.9961, 1, 0.9999 and 0.9967, to the nearest four decimal places. Whilst the properties of steam are known to deviate from ideal when close to saturation, the temperatures and pressures present in HDH systems are sufficiently low for this deviation to be negligible.

Effects of Salinity

It would be incorrect to state that the effect of salinity upon the design of HDH systems is negligible. First of all, saline feed solutions carry a risk of scaling that can greatly affect system operation and performance. However, even beyond the effects of scaling, salinity affects the energetic performance of HDH in two key ways:

1. Salinity increases the specific heat at constant pressure of water.

2. Salinity lowers the the saturation pressure of vapor.

Using the seawater correlations developed by Sharqawy *et al.* [15], we find that for a range of temperatures between 20°C and 80°C, the specific heat capacity of seawater at 35 ppm on a mass basis, is approximately 4 to 4.5% smaller than that of pure water. Salinity also causes a decrease in the saturation pressure of water. In Fig. 2-5, the saturation pressure is plotted for pure water and water within a seawater solution of 35 000 ppm. The difference in saturation pressure (seawater to pure water) is approximately -2% over the temperature range of interest for HDH. This will become

important when evaluating the impact of salinity upon the shape of the saturation curve on humidity ratio and enthalpy diagrams in Section 2.3.

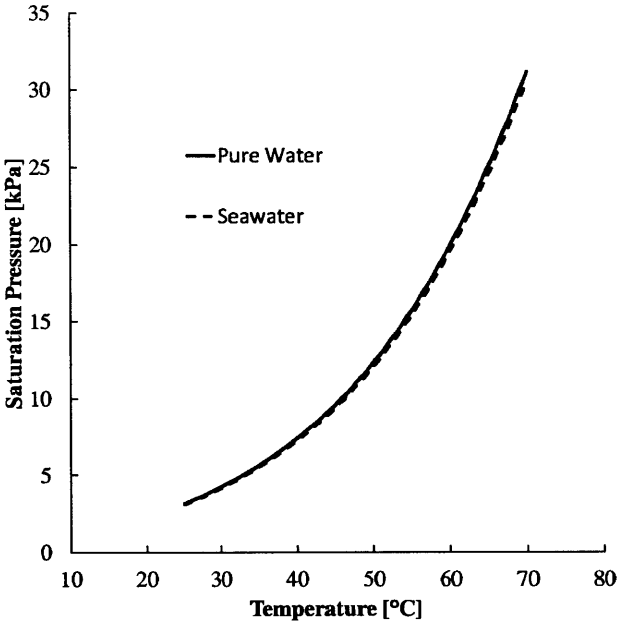

Figure 2-5: Saturation pressure of moist air when at equilibrium with pure water and seawater

The effects of salinity upon the specific heat of brine and the saturation humidity of air are less than 5%. The methodology involved in designing an energy efficient HDH system based upon a pure feed stream is the same as if the stream were to be saline. As such, the consideration of a pure water HDH system is a useful, simpler and yet reasonably accurate means of developing a design methodology.

Saturation Curve Process Path

The saturation curve methodology for the analysis of HDH systems involves approximating the process path of the moist carrier gas during humidification *or* dehumidification as the saturation curve. At saturation, the temperature and vapor pressure are not independent. Consequently, the parametric space that the moist carrier gas may occupy is reduced to the saturation curve.

Making the above four approximations simplifies the analysis of HDH considerably.

Leaving salinity aside, the state of the water at any point in the system is fully specified by its temperature. The state of the gas mixture is also fully specified by its temperature, since the pressure of the system is constant, and the saturation curve relates the humidity ratio to temperature. Next we describe two types of water heated open air cycles, the first without any extraction or injection and the second with one single extraction and injection of water (as in Fig. 2-1).

2.4.2 Zero Extraction Cycle

We begin by describing the the process paths of the moist air, condensate and feed streams within the dehumidifier. We fix the temperature of the inlet feed stream at $T_{\mathrm{f,D,B}}$, and also fix the top temperature of the moist air, $T_{\mathrm{ma,T}}$. Next we imagine a dehumidifier of infinite area such that the pinch point temperature difference at the top and bottom are zero. In other words $T_{\mathrm{f,D,B}} = T_{\mathrm{ma,D,B}} = T_{\mathrm{c,D,B}}$ and also $T_{\mathrm{f,D,T}} = T_{\mathrm{ma,D,T}}$. By fixing the temperature of the moist air at any point, we are also fixing its humidity, since we are approximating the process path by the saturation curve. By making these specifications, the mass flow ratio of feed to dry air becomes fixed, in order for the First Law to be satisfied for the dehumidifier. This may be seen in Fig. 2-6. At each point in the dehumidifier, the condensate is taken to be at the temperature of the saturated moist air. The dashed line in Fig. 2-6b includes the enthalpy of the moist air and of the condensate. The choice of whether the condensate is at the liquid or air temperature is insignificant since the effect of the change in enthalpy of the condensate upon the shape of the dashed line is very small. As outlined in Eq. (2.14), the shape of the saturation curve is dictated by the vapor content of the air. Since the dehumidifier is externally adiabatic, the change in enthalpy of the feed water matches the change in enthalpy of the moist air and the condensate exactly.

Since the cycle is water heated, the top temperature of the moist air is the same as the top temperature of the dehumidifier. Let us fix the inlet air temperature, $T_{\mathrm{ma,H,B}}$. We are now left with two unknowns, $T_{\mathrm{ma,H,T}}$ and $T_{\mathrm{f,H,B}}$, and one equation, the First Law for the externally adiabatic humidifier:

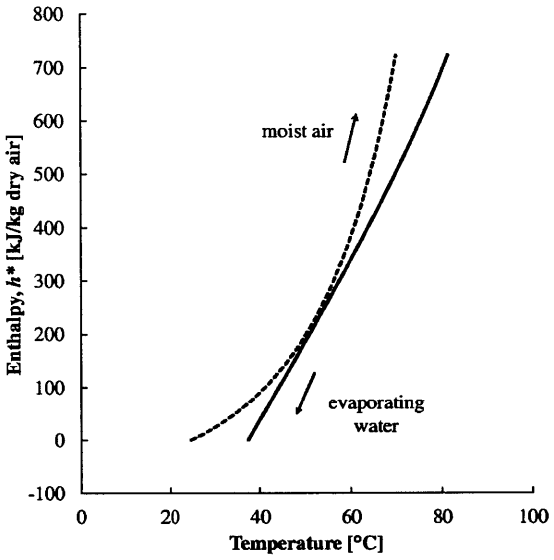

(a) Humidifier

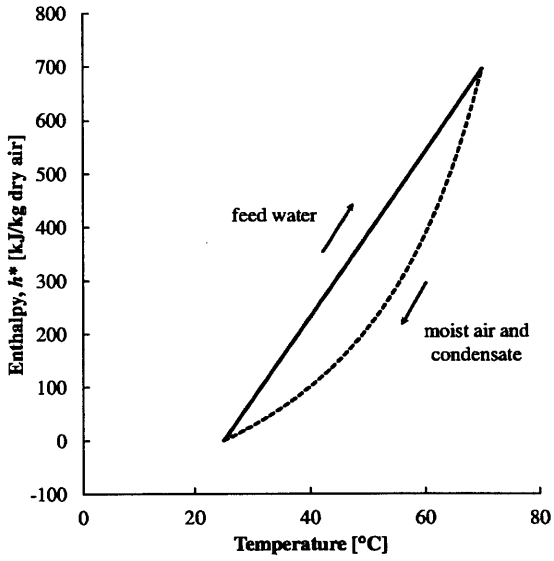

(b) Dehumidifier

Figure 2-6: Zero extraction process paths - zero pinch point temperature differences

$$h^*_{\mathrm{ma,T}} - h^*_{\mathrm{ma,H,B}} = h^*_{\mathrm{f,H,T}} - h^*_{\mathrm{r,H,B}} \tag{2.17}$$

However, by setting a pinch point temperature difference of zero in the humidifier, we obtain a final relation that closes the system of equations. At the pinch point in the humidifier, the evaporating water line must be tangent to the saturation curve. The process path of the evaporating water is close to but not exactly a straight line. The path is slightly convex due to the evaporation of water. Since the mass of water evaporated is small the curvature is not noticeable.

2.4.3 Single Extraction/Injection Cycle

Again, for this single extraction/injection cycle, we begin by considering the dehumidifier. We fix the inlet feed stream at $T_{\mathrm{f,D,B}}$ and the top temperature of the moist air, $T_{\mathrm{ma,T}}$. We set the pinch point temperature difference to be zero at the top and bottom of the dehumidifier but also at the point of injection, *i.e.* $T_{\mathrm{f,M,D}} = T_{\mathrm{ma,M,D}}$, Fig. 2-7b.

At this stage we have two equations, the First Law above and below the injection point. We also have three unknowns, the temperature of injection, $T_{\mathrm{f,M,D}}$, and the feed to dry air mass flow ratio above and below the point of injection. Moving to the humidifier, we again fix the inlet air temperature, $T_{\mathrm{ma,H,B}}$. We note that the feed temperature at the extraction point in the humidifier equals the feed temperature at the injection point in the dehumidifier. The mass flow ratio at the top of the humidifier is set by the mass flow ratio above the injection point in the dehumidifier. The mass flow ratio just below the point of extraction in the humidifier is set by the mass flow ratio below the injection point in the dehumidifier, Fig. 2-7b. We are now left with four unknown temperatures, $T_{\mathrm{ma,H,T}}$, $T_{\mathrm{f,H,B}}$, $T_{\mathrm{f,M,D}}$ and the temperature of the moist air at the feed extraction point in the humidifier, $T_{\mathrm{ma,H,M}}$. The mass flow ratio above and below the injection point in the dehumidifier are also unknown. This leaves us with six unknowns. However, we can also find six equations. First, we have four equations from the application of the first law above and below the extraction

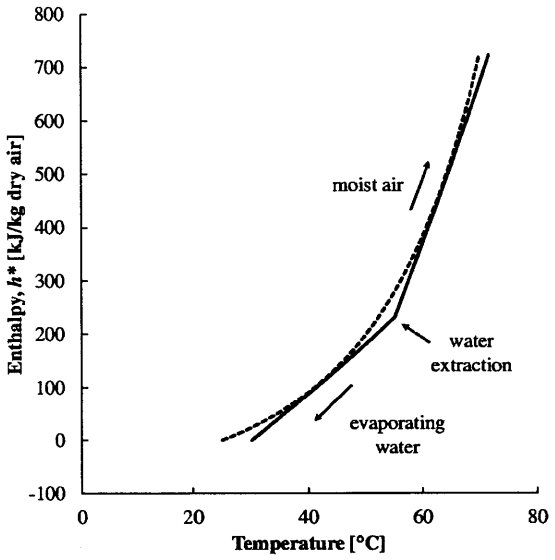

(a) Humidifier

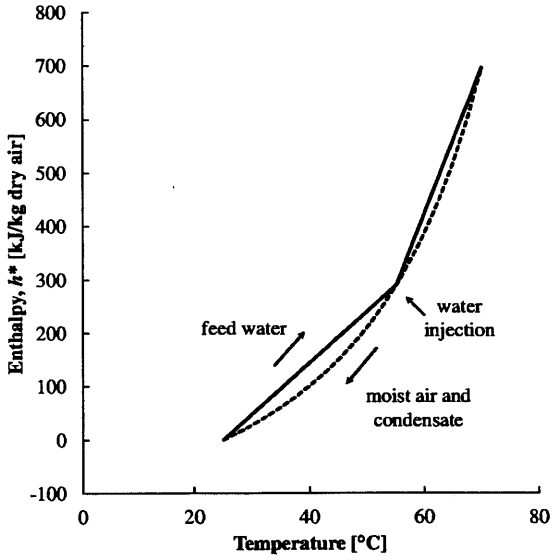

(b) Dehumidifier

Figure 2-7: Single extraction process paths - zero pinch point temperature differences

point in the humidifier and above and below the injection point in the dehumidifier. Additionally, by setting pinch point temperature differences of zero in the humidifier, we have two further equations. As in the case with zero extractions/injections, the slope of the evaporating stream must equal the slope of the saturation curve in the humidifier at the pinch points. This allows us to solve for the profiles obtained in Fig. 2-7.

2.5 Results: Explanation of the Performance Limits of HDH

In this section we return to the questions posed in Section. 2.1 and provide graphical answers. We begin by explaining how our performance metrics, GOR and RR, relate to the graphs presented in Section 2.4. To help with these explanations, it is instructive to combine Fig. 2-6 to form Figs. 2-8a and 2-8b for a zero extraction/injection system.

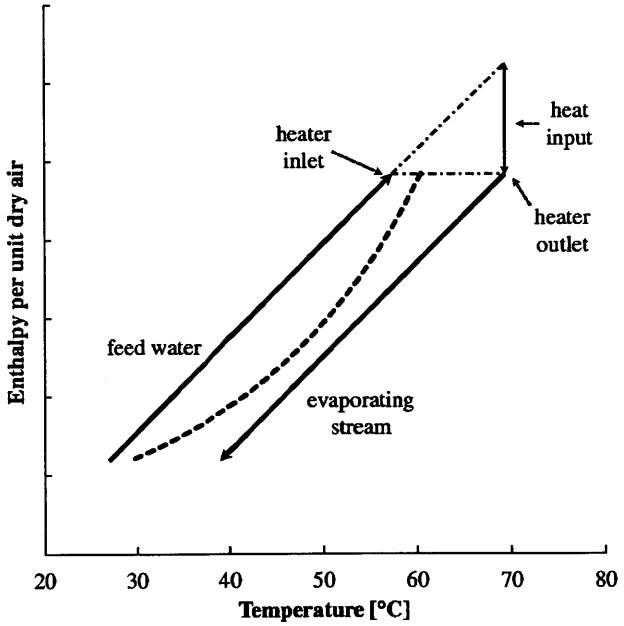

Figure 2-8: Process paths of liquid and moist air streams within a zero extraction/injection HDH system

Although Fig. 2-8 is approximative it will prove to be very illustrative in explaining trends in the performance of HDH cycles. Feed water enters the dehumidifier and is pre-heated. The moist air, in counterflow, is cooled and water vapor is condensed to form a pure product. The feed water increases in temperature within the heater. The feed is then cooled and water evaporates into the counterflow of moist air, which is heated and humidified. In this case, air enters the system at 30°C and feed enters at 27°C. The top moist air temperature is approximately 60°C.

In HDH, the latent heat required for vaporization in the humidifier is solely provided by the sensible cooling of the feed stream. A large mass flow rate of feed is required per unit of water evaporated. Thus, the water produced in an HDH system per unit of feed, in other words the recovery ratio, is low. Strictly speaking, due to evaporation, the ratio of liquid to moist air flow rate in the humidifier is not constant. However, since the mass of water evaporated is low, the liquid path (that is slightly curved in Fig. 2-6a) is well approximated by a straight line in Fig. 2-8. In Fig. 2-6b the change in enthalpy of the condensate stream has been incorporated into the curve representing changes in enthalpy of the moist air (since both streams are approximated as being at the same temperature). However, since the mass flow of condensate per unit air is small, there is little difference between the dashed lines in Fig. 2-6a and Fig. 2-6b. In Fig. 2-8 the saturation curve shown represents the path of the moist air in the humidifier and the dehumidifier.

The saturation curve on an enthalpy-temperature diagram is approximately the same as the saturation curve on an humidity-temperature diagram, scaled by h_{fg}. Therefore, the height of the saturation curve in Fig. 2-8 is proportional to the quantity of water produced per unit of dry air. Meanwhile, the ratio of feed to dry air flow is given by the slope of the liquid lines in Fig. 2-8, which may be represented by the height of the curve divided by the width. Consequently, the recovery ratio is proportional to the width of the saturation curve in Fig. 2-8.

Returning to our definition of GOR, Eq. (2.3), we are reminded that the heat input per unit mass of air is given by the change in enthalpy of the feed stream in the heater per unit mass of air, Eq. (2.18). Combining Eqs. (2.3) and (2.18) we obtain

Eq. (2.19). This change in enthalpy is easily visualized in Fig. 2-8, where $\frac{\dot{m}_{\mathrm{f,H,T}}}{\dot{m}_{\mathrm{a}}} c_{p,\mathrm{f}}$ is the slope of the feed line. The feed process path within the heater may be visualised by extending the feed line from the heater inlet to the heater outlet temperature. The further apart the heater inlet and heater outlet temperature are, the greater the heat input to the cycle.

$$h^*_{\mathrm{f,D,T}} - h^*_{\mathrm{f,H,T}} = \frac{\dot{m}_{\mathrm{f,H,T}}}{\dot{m}_{\mathrm{a}}} c_{p,\mathrm{f}} (T_{\mathrm{f,D,T}} - T_{\mathrm{f,H,T}}) \tag{2.18}$$

$$\mathrm{GOR} = \frac{\Delta\omega h_{\mathrm{fg}}}{\frac{\dot{m}_{\mathrm{f,H,T}}}{\dot{m}_{\mathrm{a}}} c_{p,\mathrm{f}} (T_{\mathrm{f,D,T}} - T_{\mathrm{f,H,T}})} \tag{2.19}$$

2.5.1 Impact of a Single Extraction/Injection upon GOR and RR

Consider the water produced per unit of carrier gas. The top temperature of the moist air is fixed at 70°. Due to our choice of pinch point temperature differences of zero in the humidifier and dehumidifier, the temperature reached by the saturated moist air at the exit of the dehumidifier equals the inlet feed temperature. Consequently, the water produced per unit mass (or mole) of carrier gas in the dehumidifier is the same for the zero and single extraction systems.

The implementation of a single extraction results in an improvement of the energetic performance (GOR) simply because it allows a smaller temperature difference across the heater. Also, if the temperature difference across the heater is reduced, the temperature difference between the rejected stream and the feed stream will also reduce according to a First Law energy balance upon the system. For the single extraction system of Fig. 2-7, the GOR is 14 compared to the zero extraction system of Fig. 2-6, where the GOR is 3.5.

In essence, by employing an extraction/injection, the process paths of the feed provide a better piecewise linear approximation of the saturation curve. From a second law perspective we are really saying that by improving the matching of the saturation curve and the liquid lines we are distributing the driving forces for heat

and mass transfer throughout the system in a more even fashion, see [17] and [18]. This reduces the stream to stream temperature differences in the humidifier and dehumidifier, thus minimizing the heat requirements of the cycle. Comparing Fig. 2-7 to Fig. 2-6, we can see that the employment of a single extraction greatly reduces the average driving force for heat transfer (the stream to stream temperature difference).

Mass transfer is also important process within HDH, driven by differences in vapor concentration. At the liquid-air interface in the humidifier, and the heat-exchanger-surface-air interface in the dehumidifier, the air is locally saturated at a temperature close to that of the the liquid, assuming that air is the dominant heat transfer resistance. By plotting the bulk humidity of the air stream versus the saturation humidity at the liquid temperature, we may visualize the concentration difference that drives mass transfer in the humidifier and the dehumidifier, Fig. 2-9.

From Fig. 2-9 it is clear that the implementation of an extraction/injection greatly reduces the average driving force for mass transfer (concentration difference) within both the humidifier and the dehumidifier. In Fig. 2-9a it is interesting to note the very large difference in humidity ratio at the top of the humidifier. This is because a small temperature difference between the bulk air and the liquid at high temperature results in a large difference in humidity ratio due to the steep slope of the saturation curve at high temperatures.

Finally, we turn to the recovery ratio, RR. We have already said that for fixed top and bottom moist air temperatures, the water produced per unit of carrier gas is fixed. Now, the recovery ratio is given by the mass of product divided by the mass of feed, or in other terms, the mass of product per unit mass of dry air divided by the mass of feed per unit mass of dry air, Eq. (2.20). The mass flow rate of feed per unit mass of carrier gas at the inlet to the HDH systems in Fig. 2-6b and Fig. 2-7b is given by the slope of the feed line at the inlet. Clearly the slope is lower in the system with one single extraction and consequently the recovery ratio is higher.

$$\mathrm{RR} = \frac{\dot{m}_{\mathrm{p}}}{\dot{m}_{\mathrm{f,H_2O}}} = \frac{\dot{m}_{\mathrm{p}}}{\dot{m}_{\mathrm{da}}} \frac{\dot{m}_{\mathrm{da}}}{\dot{m}_{\mathrm{f,H_2O}}} \tag{2.20}$$

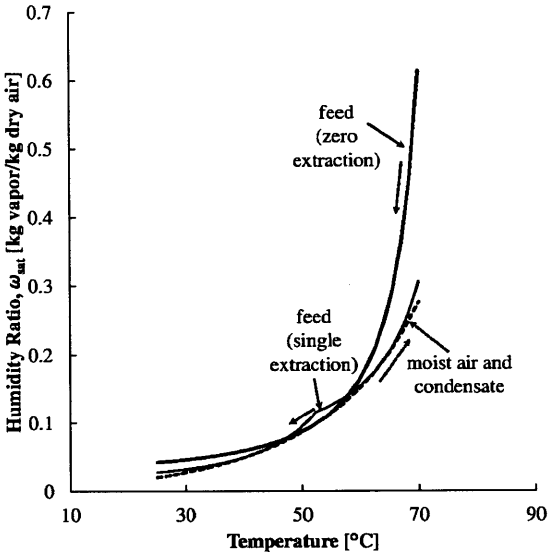

(a) Humidifier

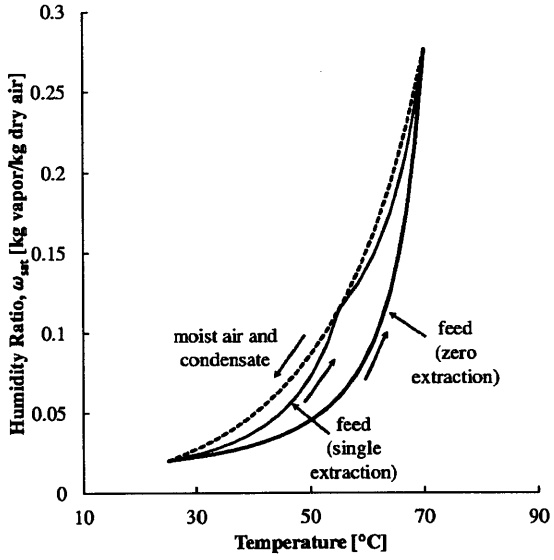

(b) Dehumidifier

Figure 2-9: Saturation humidity ratio at the moist air bulk temperature and the feed temperature for zero and single extractions

2.5.2 Effect of the Cycle Temperature Range

By temperature range, we mean the difference in the top moist air temperature in the cycle and the bottom moist air temperature (*i.e.* at the humidifier inlet). In general, the moist air inlet temperature will be fixed by the temperature of the surroundings whilst the top moist air temperature is a design parameter. In Fig. 2-10 the effect of the top moist air temperature upon the GOR and the RR is plotted.

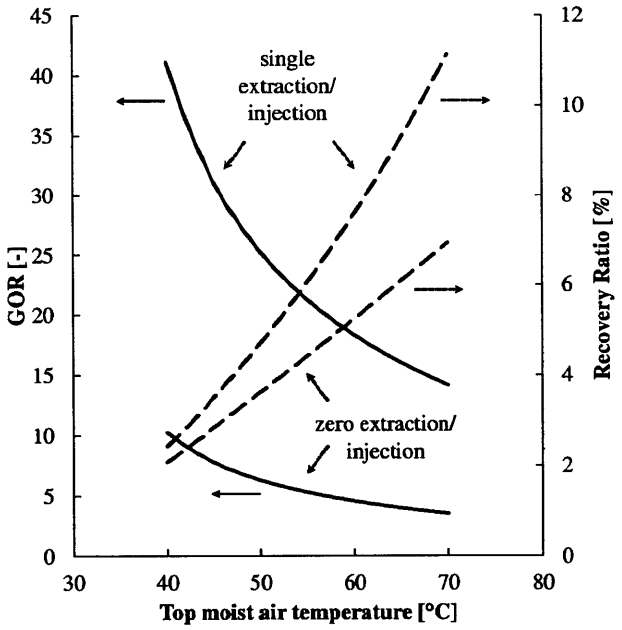

Figure 2-10: Effect of the top moist air temperature upon GOR and RR, $T_{\mathrm{f,D,B}} = T_{\mathrm{ma,H,B}} = 25°\mathrm{C}$

As the top moist air temperature decreases, the GOR increases. Simply said, this is because our piecewise linear approximation of the saturation curve becomes more accurate when considering a cycle that spans a smaller temperature range. Fig. 2-10 also indicates that the RR decreases as the top moist air temperature is lowered. This is because the mass flow of feed per unit mass of air (dictated by the slope of the feed line at the inlet, see Fig. 2-6b) decreases at a faster rate than the mass flow of product water per unit mass of air. To make this intuitively obvious, we may consider Fig. 2-11.

According to Eq. (2.14), the saturation curves on an humidity-temperature and on

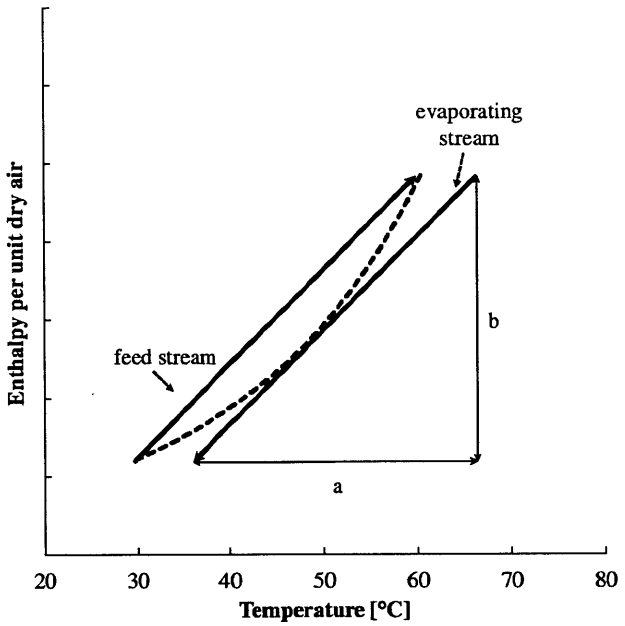

Figure 2-11: Illustration of the effect of decreasing top air temperature upon the recovery ratio

an enthalpy-temperature diagram are scaled copies of each other. Therefore, distance b on Fig. 2-11 is proportional to the change in humidity of the carrier gas in the dehumidifier, and consequently the water produced per unit of air. As the top moist air temperature decreases, the length of b decreases and the length of a decreases [2]. Since the slope of the feed line is given by $\frac{b}{a}$, the rate of water production per unit mass of air, given by b, decreases at a faster rate than the ratio of feed to air flow, given by $\frac{b}{a}$. Hence, the recovery ratio must decrease, according to Eq. (2.20).

In Fig. 2-12 we investigate the effect of increasing the feed and moist air inlet temperatures upon the GOR and RR, for a fixed top moist air temperature. As the inlet streams' increase in temperature, the water produced decreases slowly. (Due to the exponential shape of saturation curve the quantity of water produced is much more sensitive to the top than the bottom temperature.) Meanwhile, the heat input per unit of air decreases more rapidly, resulting in an improvement of the energetic performance and the GOR. Applying similar arguments to those outlined through

[2]Note that the feed line and the evaporating line must be parallel as the liquid to air mass flow ratios are equal in the humidifier and dehumidifier

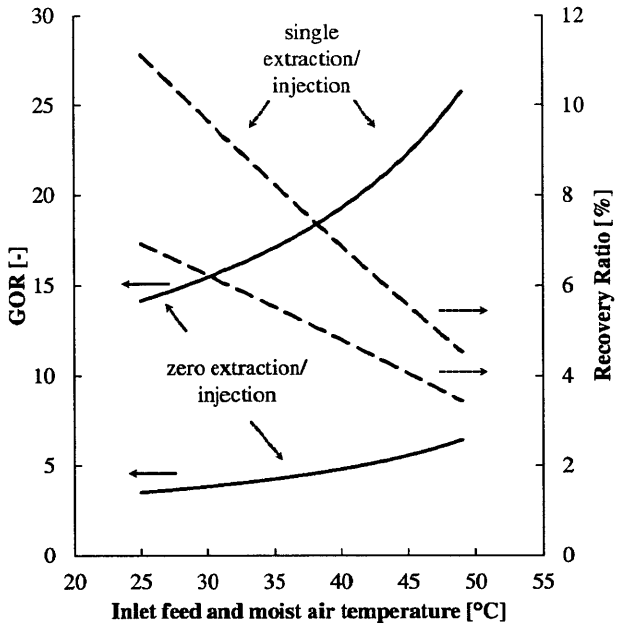

Figure 2-12: Effect of the inlet feed and saturated moist air inlet temperature upon GOR and RR, $T_{\mathrm{ma,D,T}} = T_{\mathrm{ma,H,T}} = 70°\mathrm{C}$

the use of Fig. 2-11, it may be shown that the RR must also decrease as the bottom inlet streams' tempeature increases.

2.5.3 Effect of Component Size

In a bi-fluid heat exchanger, the driving force for heat transfer is dictated by temperature differences between the two streams. For a fixed duty, *i.e.* heat transfer rate, a smaller heat exchanger will require larger driving force (assuming constant heat transfer coefficients). The pinch point temperature difference (PPTD) is defined as the minimum temperature difference between the two streams. It is somewhat characteristic of the driving force for heat transfer. Following this line of argument, to achieve a fixed rate of heat transfer within a heat exchanger, the pinch point temperature difference is somewhat indicative of the heat exchanger size required. As the PPTD increases, a smaller heat exchanger is required and vice versa.

The above arguments may also be applied for a mass exchanger. The driving force for mass transfer is given by a concentration difference. A pinch point concentration

difference (PPCD) would be somewhat analogous to the PPTD in a heat exchanger.

In a heat and mass exchanger (HMX), such as an humidifier or dehumidifier, there are two driving forces, temperature difference and concentration difference. The size of the heat and mass exchanger, for a fixed heat and mass transfer rate is therefore somewhat related to the PPTD and the PPCD. In the case of the saturation curve method of HDH analysis, the temperature and humidity of the moist air are always linked by the equation describing the saturation curve. Hence, by specifying a PPTD between a fluid and moist air stream, we are in fact also specifying a PPCD between the fluid and the moist air stream.

We know that the saturation vapor concentration is an exponential function of temperature. Therefore, the PPCD and PPTD are not linearly related. In fact, depending upon the temperature at which we specify the PPTD, the PPCD could be very small (at low temperature) and very large (at high temperature). In other words, by increasing the PPTD it is unclear to what extent the heat and mass exchanger size is decreasing. What we *can* say, is that for fixed top and bottom moist air temperatures, increasing the PPTD in the humidifier or dehumidifier will decrease the HMX size required for a fixed water output.

For illustrative purposes a graphical representation of HDH cycles with zero and a single extraction/injection for pinch point temperature differences of 2 K in the humidifier and dehumidifier are provided in Fig. 2-13 and also Fig. 2-14. Note how, due to the shape of the saturation curve, there are pinch points at the inlet and outlet of the dehumidifier but within the humidifier.

In Fig. 2-15 the GOR is plotted versus PPTD, setting the temperature difference at each pinch point to be equal at all pinch points. Again the inlet streams' temperature is 25°C and the top moist air temperature is 70°C.

Unsurprisingly, as the PPTD increases, the GOR decreases due to an increasing temperature difference across the heater. Interestingly, there exists a critical value of PPTD beyond which there is no advantage in employing an extraction and injection of water from the humidifier to the dehumidifier. This effect may be explained by considering a plot of the feed temperatures at which the pinch points occur in the

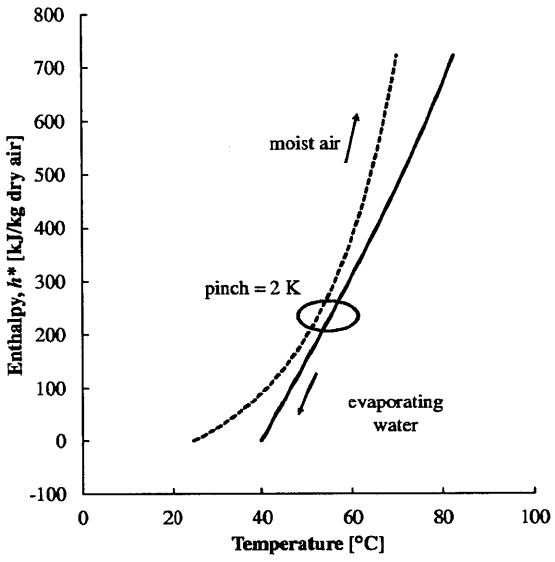

(a) Humidifier

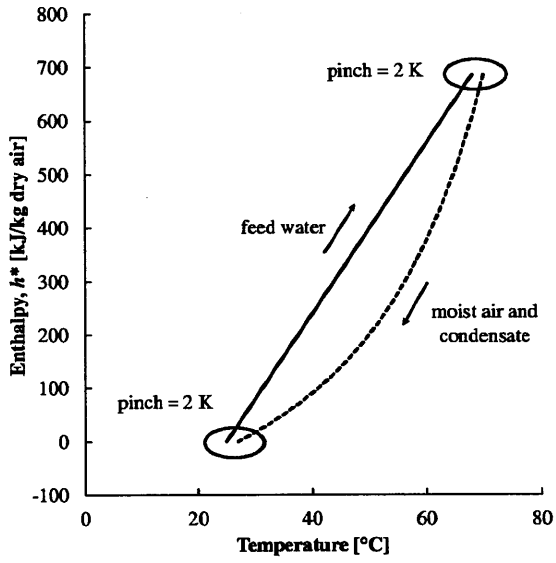

(b) Dehumidifier

Figure 2-13: Zero extraction process paths - PPTD = 2 K

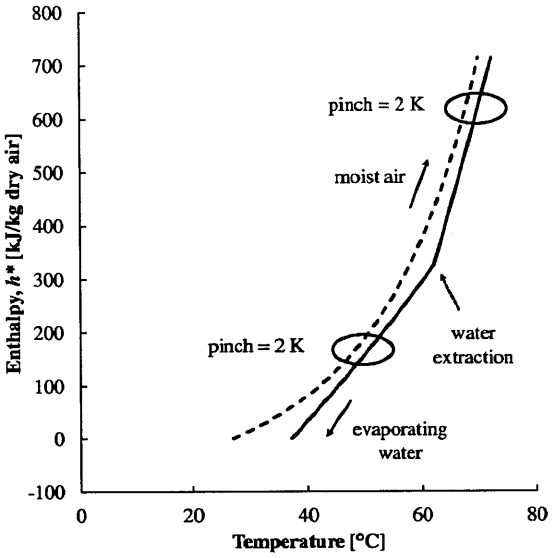

(a) Humidifier

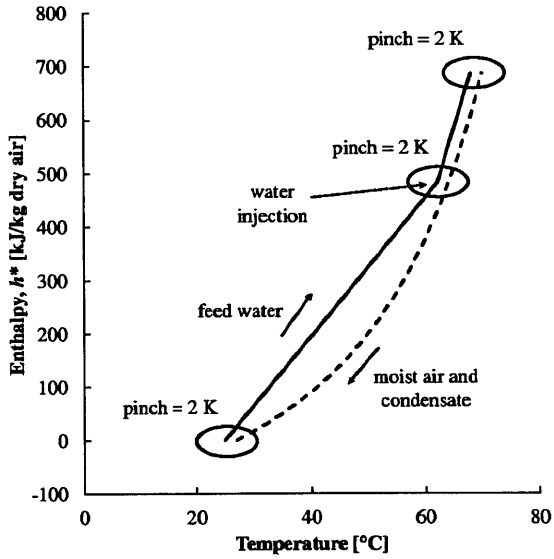

(b) Dehumidifier

Figure 2-14: Single extraction process paths - PPTD = 2 K

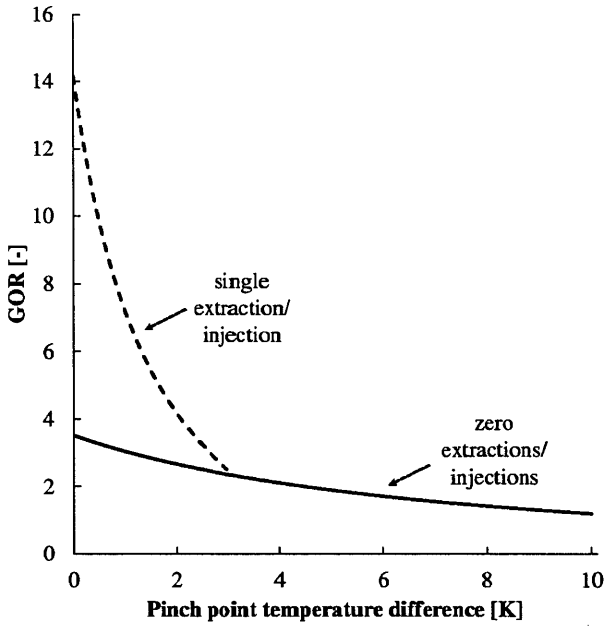

Figure 2-15: GOR versus temperature pinch within the humidifier and dehumidifier for cases with zero and a single water extraction

humidifier and the extraction temperature versus the PPTD, Fig. 2-16.

As the PPTD increases, the optimal extraction temperature increases. Once the top pinch point reaches the top moist air temperature, no further advantage may be obtained via extraction/injection.

A second observation arising from Fig. 2-15 is that the GOR of a system with a single extraction/injection is more sensitive to changes in PPTD than a system with zero extractions. In a system with zero extractions and a small PPTD, Fig. 2-13, the PPTD is not a very good measure of average driving forces within the system. Rather, the average driving force is dictated by mismatch in shape between the saturation curve and the feed streams. Increasing the PPTD therefore has a weak effect upon the temperature difference obtained across the heater. By contrast, in Fig. 2-14a and Fig. 2-14b, the PPTD is much more representative of the mean temperature difference between the streams. This is because much of the mismatch in shape between the liquid and moist air paths has been eliminated by the single extraction/injection. Consequently, the temperature difference across the heater is much more sensitive to

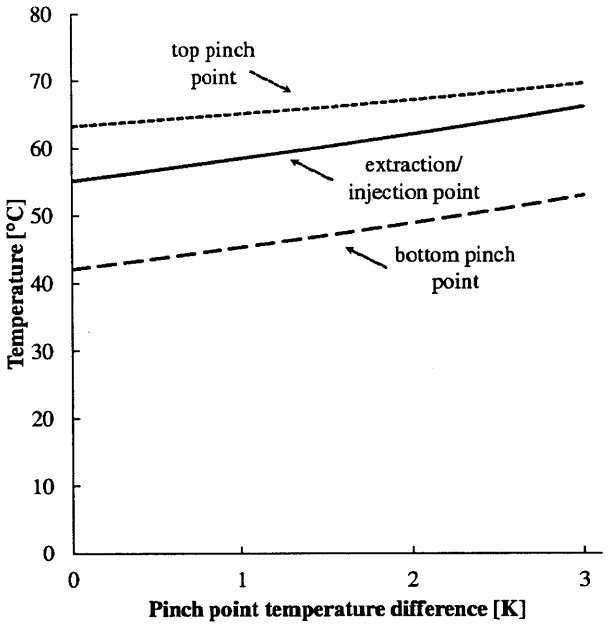

Figure 2-16: Evaporating water temperature in the humidifier at the high temperature pinch point, the water extraction point and the low temperature pinch point - all versus PPTD in the humidifier and dehumidifier

the PPTD.

Finally, in Fig. 2-17 we plot the RR versus the PPTD. As with the GOR, the RR decreases with increasing PPTD. As PPTD increases, the moist air temperature at the outlet of the dehumidifier increases, as does its humidity. Consequently, the mass flow rate of water produced per unit mass of air decreases. Additionally, the slope of the liquid lines must increase, meaning that the mass flow rate of feed per unit mass of air must increase. Thus, the mass of water produced per mass of feed must decrease, again according to Eq (2.20).

2.5.4 Impact of Salinity upon HDH Design and Performance

The above analysis of an HDH cycle, done neglecting the effects of salinity, gives an intuitive insight into the coupling between the humidifier and dehumidifier. At this stage, it is worth pointing out how the analysis would have differed had seawater properties been taken into account.

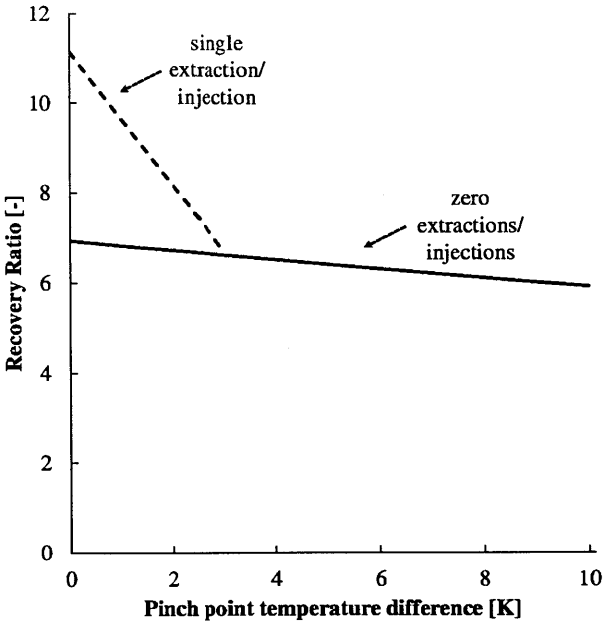

Figure 2-17: Recovery ratio versus temperature pinch within the humidifier and dehumidifier for cases with zero and a single water extraction/injection

The first difference is the smaller value of specific heat at constant pressure of the feed water in a system with saline feed. At a salinity of 35 000 ppm, the specific heat of seawater is about 4.5% smaller than that of pure water. If the same feed to air mass flow ratio was chosen for a system with such saline feed, the slope of the feed stream in the dehumidifier and the evaporating stream in the humidifier would decrease by about 4.5%. To counteract this, and to achieve the same matching of the process paths in the humidifier and dehumidifier, the mass flow ratio of feed to dry air would have to be increased by about 4.5%. By adjusting the mass flow rate the product of mass flow rate and specific heat capacity is held constant and this effect of salinity is largely negated.

Seawater salinity will reduce the slope of the saturation curve within the humidifier, due to the lower vapor pressure of seawater compared to pure water at the same saturation temperature. If the same PPTD is to be maintained as in the system with pure feed, the evaporating feed line in Fig. 2-8 will shift to the right, resulting in a larger temperature difference across the heater.

In a system with saline feed water, the properties of the evaporating stream within the humidifier will vary due to changing salinity. However, since the recovery ratio of HDH cycles is very low (less than 12% of the feed water is evaporated and subsequently condensed), the change of salinity due to concentration of the brine in the humidifier will be very small. In other words, if we consider the effect of salinity upon specific heat to be a second order effect (4.5%), then the effect of changing salinity due to evaporation would be a third order effect. In a system with a single extraction/injection, the salinity of the brine introduced from the humidifier to the dehumidifier at the midpoint would be slightly different from the salinity of the feed just before the dehumidifier injection point.

2.6 Conclusions

The coupling between the humidifier and dehumidifier makes analysis of HDH system performance challenging. In this chapter, we have developed a graphical method that enables evaluation of the thermal performance (GOR) and water recovery of an open air HDH system. By limiting the parametric space that may be occupied by the state of a moist carrier gas to the saturation curve, the analysis is simplified. This method is applicable to cycles both with and without extraction/injection from the humidifier to the dehumidifier. The main conclusions arising from this chapter are as follows:

1. A graphical method of analysis has been developed, which facilitates the exact assessment of the role the top and bottom moist air temperatures and the feed to air mass flow rate ratio upon system performance.

2. This method also facilitates the exact assessment of the role of injection and extraction in improving the thermal performance of an HDH system.

3. As the temperature range of an HDH cycle increases, the GOR decreases since the piecewise linear approximation, by the liquid streams, of the exponential saturation curve is a poorer match.

4. As the pinch point temperature difference increases, the GOR and the recovery ratio decrease.

5. The recovery ratio of an HDH system is limited by the fact that a large mass flow of hot brine is required at the humidifier inlet to provide the sensible heat necessary to supply the latent heat of vaporization.

6. A single extraction/injection improves energetic performance (GOR) by improving the matching of shape between the saturation curve and the quasi-linear feed streams.

7. There exists a critical pinch point temperature difference beyond which there is no advantage to extracting and injecting water from the humidifier into the dehumidifier.

THIS PAGE INTENTIONALLY LEFT BLANK

Chapter 3

Analysis of Reversible Ejectors and Definition of an Ejector Efficiency

Ronan K. McGovern, G. Prakash Narayan, John H. Lienhard V

Abstract

Second Law analyses of ejector performance have rarely been conducted in literature. Many measures of ejector efficiency have not always been clearly defined and the rationale underlying and justifying current performance metrics is often unclear. One common means of assessing performance is to define a thermodynamically reversible reference process against which real processes may be benchmarked. These reversible processes represent the thermodynamic limit of real ejector performance. In this chapter, parameters from real and reversible processes are compared and performance metrics are defined. In particular, the entrainment ratio of real devices is compared to the reversible entrainment ratio and denoted the reversible entrainment ratio efficiency. An efficiency comparing the ejector performance to that of a turbine-compressor system is also investigated, as is an exergetic efficiency. A rigorous analysis of performance metrics reported in the literature is undertaken. Graphical illustrations are provided to support intuitive understanding of these metrics. Analytical equations are also formulated for ideal-gas models. The performance metrics are then applied to existing experimental data to illustrate the difference in their numerical values. The reversible entrainment ratio efficiency η_{RER} is shown to always be lower than the turbine-compressor efficiency η_{TER}. For general air-air and steam-steam ejectors, the exergetic efficiency η_X is very close in numerical value to the reversible entrainment ratio efficiency, η_{RER}.

Nomenclature

Symbols

c_p	specific heat capacity at constant pressure [kJ/kg·K]
ER	entrainment ratio [-]
h	specific enthalpy [kJ/kg]
$\tilde{h}$	specific molar enthalpy [kJ/kmol]
$h_{\mathrm{E,D}}$	specific enthalpy of the entrained fluid at the discharge [kJ/kg]
$h_{\mathrm{M,D}}$	specific enthalpy of the motive fluid at the discharge [kJ/kg]
j	dissipation [J]
$\dot{m}$	mass flow rate [kg/s]
M	molar mass [kg/kmol]
$\dot{N}$	molar flow rate [kmol/s]
p	partial pressure [bar or kPa]
P	absolute pressure [bar or kPa]
$\dot{Q}$	rate of heat transfer [W]
R	gas constant [kJ/kg·K]
RER	Reversible Entrainment Ratio [-]
s	specific entropy [kJ/kg·K]
$\tilde{s}$	specific molar entropy [kJ/kmol·K]
$\dot{S}_{gen}$	entropy generation rate [kW/K]
$\bar{s}_{gen}$	dimensionless entropy generation [-]
T	temperature [°C or K]
v	specific volume [m^3/kg]
x	dryness fraction of steam [-] or specific exergy [J/kg]
y	useful work done [J]

Greek

γ	ratio of specific heats
Δ	change
η	efficiency [-]

Π_c	compression ratio (P_D/P_E) [-]
ϕ	relative humidity [-]
ω	absolute humidity [kg H_2O/kg carrier gas]
ξ	ratio of moles of vapor to moles carrier gas [-]

Subscripts

c	compression
cg	carrier gas
comp	compressor
D	discharge fluid
E	entrained fluid
f	saturated liquid
g	saturated vapour
irrev	associated with irreversible dissipation
M	motive fluid
NE	nozzle exit
q	associated with heat transfer
RDP	reversible discharge pressure
RER	reversible entrainment ratio
RHE	reversible heat engine
s	isentropic
TER	turbine-compressor entrainment ratio
turb	turbine
vap	vapor
X	exergetic
0	ambient

Superscripts

rev	reversible
sat	saturated

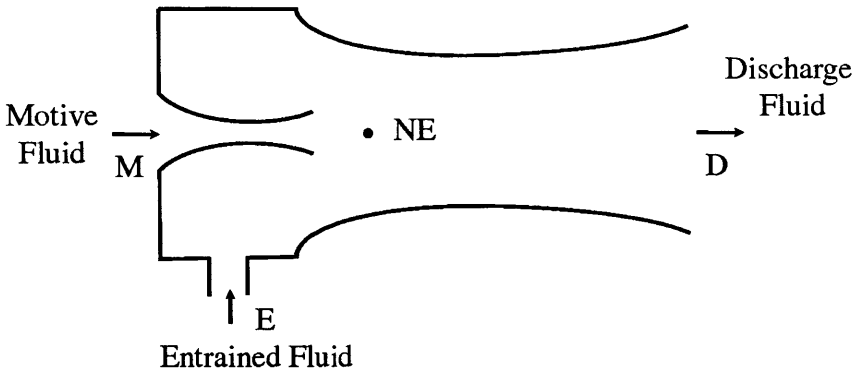

Figure 3-1: Schematic diagram of a steady flow ejector

3.1 Introduction

Steady flow ejectors are devices without moving parts that typically combine two fluids, one of high total pressure and one of low total pressure, to obtain a fluid at an intermediate total pressure at the discharge. The fluid with high total pressure, known as the motive fluid, is expanded through a nozzle to high velocity and low pressure (point NE in Fig.3-1). The low pressure at the nozzle exit provides the driving force for suction of the low pressure fluid, known as the entrained fluid, at pressure P_{E}, such that $P_{\mathrm{M}} > P_{\mathrm{E}} > P_{\mathrm{NE}}$. The motive and entrained streams undergo mixing, brought about by shear forces between the fluids, before the resulting mixture is diffused to attain the discharge pressure, P_{D}, Fig. 3-1.

The most intuitive although approximative manner to comprehend ejector operation is to analyse performance using simple 1-D analyses. Examples of excellent work in this regard have been done by Elrod [19], Keenan *et al.* [20], Chou *et al.* [21] and Arbel *et al.* [22]. Ejectors are relatively simple in design and can provide reliable operation at low capital cost. These advantages have led to ejectors being used in processes requiring the drawing of a vacuum (*e.g.* extraction of non-condensible gases from condensers) or the compression of a gas (*e.g.* within refrigeration cycles). In thermal desalination, ejectors are commonly employed to compress and entrain water vapor. Such devices are known as thermal vapor compressors. The increased use of thermal vapor compressors for energy intensive processes of thermal desalination,

in particular multi-effect distillation [23–26], has brought about renewed interest in the efficiency of ejectors. Despite the interest in energy efficiency, scant attention has been paid to the definition and justification of the utility of ejector performance metrics employed to date. Bulusu *et al.* [1] presented common measures of ejector performance, whilst Arbel *et al.* [22] performed an analysis of entropy generation within ejectors. Nonetheless, there remains no universally accepted efficiency to characterise and compare the performance of such devices.

In this chapter, ejector performance is evaluated by benchmarking real ejector processes against carefully defined thermodynamically reversible processes. In Section 3.2, a systematic methodology is presented to define such processes. One important parameter arising from this analysis is the reversible entrainment ratio, *i.e.* the maximum theoretical entrainment ratio achievable by a thermodynamically reversible ejector. The variation in the reversible entrainment ratio with an ejector's operating conditions is investigated in Section 3.3. Then, in Section 3.4 ejector performance metrics are explained and justified by means of analytical equations or graphical methods. Finally, in Section 3.5, the numerical values of these metrics are computed for experimental data available in open literature. The exergetic efficiency η_X of an ideal gas ejector with inlet fluids at the same temperature is shown to be identical to the reversible entrainment ratio efficiency η_{RER}.

3.2 Description of Reversible Ejector Processes

This section establishes a basis for benchmarking real device performance against the performance of ideal, thermodynamically reversible processes. In order to effectuate this comparison, the following steps are necessary:

1. Identify the input quantities, output quantities and equations describing a thermodynamically reversible process.

2. Define a thermodynamically reversible reference process, against which real processes may be compared.

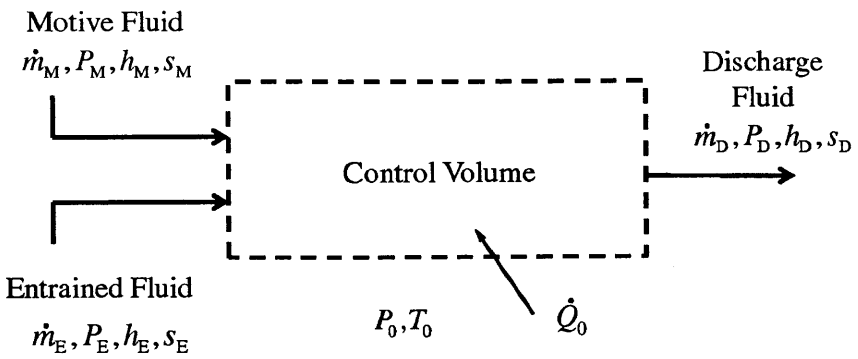

Figure 3-2: Control volume for an ejector process

3. Develop a performance metric based on a comparison of parameters between the real and reversible processes. (3.4)

A control volume model of an ejector process is presented in Fig. 3-2. The inlet stream of higher pressure is known as the motive flow, the low pressure inlet stream is termed the entrained flow and the outlet stream is termed the discharge flow. The control volume in both real and reversible cases is considered externally adiabatic ($\dot{Q}_0 = 0$). Due to the high flow speeds within ejectors, the rate of heat loss from the device to ambient is taken to be small relative to changes of enthalpy of the streams within. The nomenclature of Fig. 3-2 shall henceforth be used in refering to the mass flow rates and state properties of inlet and outlet streams. All analyses shall consider only equilibrium states of inlet and outlet fluids where the fluids are at conditions of stagnation (zero kinetic energy). Thus, all temperatures and pressures are total rather than static temperature and pressures.

3.2.1 Equations Describing a Thermodynamically Reversible Process

Taking a control volume approach, the First and Second Laws of Thermodynamics may be written for a real ejector process involving pure and identical fluids at the ejector inlet:

First Law of Thermodynamics for an adiabatic process:

$$\dot{m}_{\mathrm{M}} h_{\mathrm{M}} + \dot{m}_{\mathrm{E}} h_{\mathrm{E}} = \dot{m}_{\mathrm{D}} h_{\mathrm{D}} \tag{3.1}$$

$$h_{\mathrm{M}} + \mathrm{ER} \cdot h_{\mathrm{E}} = (1 + \mathrm{ER}) h_{\mathrm{D}} \tag{3.2}$$

The entrainment ratio, ER is defined as the ratio of entrained mass flow to motive mass flow,

$$\mathrm{ER} = \frac{\dot{m}_E}{\dot{m}_M} \tag{3.3}$$

Second Law of Thermodynamics for an adiabatic process:

$$\dot{m}_{\mathrm{M}} s_{\mathrm{M}} + \dot{m}_{\mathrm{E}} s_{\mathrm{E}} + \dot{S}_{\mathrm{gen}} = \dot{m}_{\mathrm{D}} s_{\mathrm{D}} \tag{3.4}$$

$$s_{\mathrm{M}} + \mathrm{ER} \cdot s_{\mathrm{E}} + \frac{\dot{S}_{\mathrm{gen}}}{\dot{m}_{\mathrm{M}}} = (1 + \mathrm{ER}) s_{\mathrm{D}} \tag{3.5}$$

Noting that no entropy is generated during a reversible process, the equations for an adiabatic and reversible process may be formulated as follows:

$$h_{\mathrm{M}} + \mathrm{RER} \cdot h_{\mathrm{E}} = (1 + \mathrm{RER}) h_{\mathrm{D}}^{\mathrm{rev}} \tag{3.6}$$

$$s_{\mathrm{M}} + \mathrm{RER} \cdot s_{\mathrm{E}} = (1 + \mathrm{RER}) s_{\mathrm{D}}^{\mathrm{rev}} \tag{3.7}$$

Reversible entrainment ratio RER is defined as the ratio of entrained mass flow to motive mass flow in the reversible process:

$$\mathrm{RER} = \left(\frac{\dot{m}_E}{\dot{m}_M} \right)^{\mathrm{rev}} \tag{3.8}$$

For a pure fluid, the thermodynamic state is fully specified at the control volume inlets and outlet once two state properties (*i.e.* h and s) are known. An equation

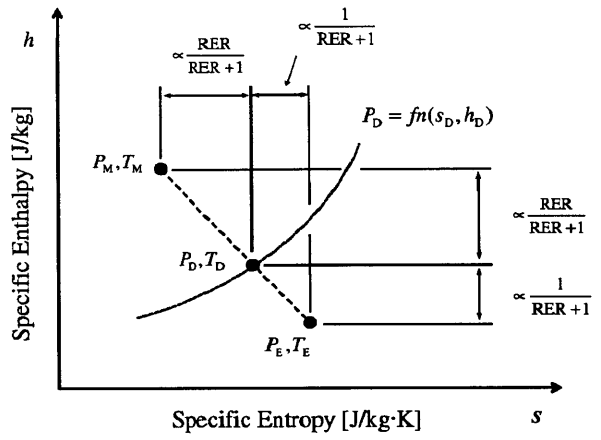

Figure 3-3: Graphical representation of the reversible entrainment ratio

of state may be written relating the temperature T or the pressure P to the specific enthalpy and entropy. The specific enthalpy and entropy of the discharge stream is simply the mass weighted average of the inlet streams, see Fig. 3-3. Of course, according to Eq. (3.6) and (3.7), the entrainment ratio, ER, is the mass ratio relevant to this weighting. Hence, on a diagram of specific enthalpy versus specific entropy, the discharge fluid state must lie on the line joining the states of the inlet fluids, as shown in Fig. 3-3. The next step is to define the different possible reversible reference processes.

3.2.2 Definition of Thermodynamically Reversible Reference Processes

Six state variables and one mass flow rate ratio describe the process of Fig. 3-2. For a real process there are two equations, Eq. (3.2) and Eq. (3.5), including one further unknown, $\frac{\dot{S}_{gen}}{\dot{m}_M}$. This value of this entropy generation term is dictated by the quality of design of the device within the control volume. For a reversible process, there are two associated equations, Eq. (3.6) and Eq. (3.7). Consequently, given 7 variables

and 2 equations, there are five degrees of freedom that must be specified in order to define a reversible reference process. There are therefore 21 (7-choose-5) different ways in which a reference process could be defined. A select number of combinations are discussed in the following subsections.

Reversible Discharge Pressure Reference Process

In a paper elucidating the sources of irreversibilty within steady flow ejectors, Arbel *et al.* [22] investigated ejector performance in great detail by comparing real processes to a reversible reference process, described in Table 3.1:

Table 3.1: Reversible discharge pressure process

Fixed	Output
$P_{\mathrm{E}} = P_{\mathrm{E}}^{\mathrm{rev}}$	$P_{\mathrm{D}}^{\mathrm{rev}}$
$T_{\mathrm{E}} = T_{\mathrm{E}}^{\mathrm{rev}}$	$T_{\mathrm{D}}^{\mathrm{rev}}$
$P_{\mathrm{M}} = P_{\mathrm{M}}^{\mathrm{rev}}$	
$T_{\mathrm{M}} = T_{\mathrm{M}}^{\mathrm{rev}}$	
$\mathrm{ER} = \mathrm{RER}$	

In essence, Arbel *et al.*'s reference processes asks: for fixed inlet fluid states and a fixed entrainment ratio, what is the maximum discharge pressure achievable if the process is reversible? On an $h - s$ diagram, Arbel's process may be represented as:

Discharge enthalpy in both the real and reference case is a weighted average of the inlet fluid enthalpies. Since by definition of this reference process, the real and reversible entrainment ratios are equal, the discharge specific enthalpy is also equal in the real and reversible cases, Eq. (3.2). In the real process, entropy is generated and thus the discharge specific entropy is greater than the weighted mean of the entropy of the inlet streams.

For applications where the inlet states are fixed, as is the relative mass flow of motive and entrained fluid available, this reference process may be employed to determine how close the actual discharge pressure achieved is to the reversible limit.

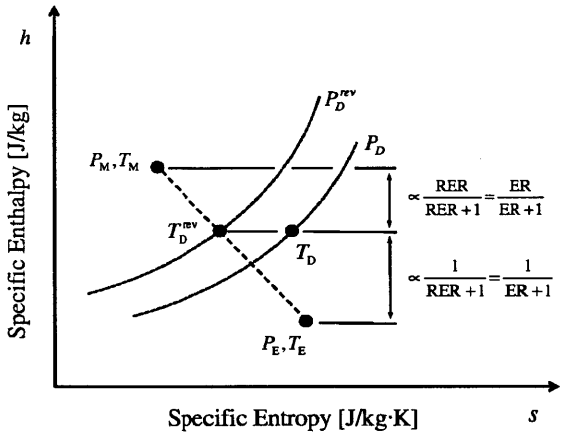

Figure 3-4: Graphical representation of the reversible discharge pressure reference process

Reversible Entrainment Ratio Reference Process

In many situations, the inlet states to the ejector are known, as is a desired discharge pressure[1]. Such is the case when one has steam available at a fixed state and wishes to compress vapor, also at a known state, to a desired pressure. The efficiency of the ejector will determine the mass flow of vapor one can entrain per unit mass flow of steam (*i.e.* the entrainment ratio). In such a scenario, the reference process described in Table 3.2 is of relevance:

Table 3.2: Reversible entrainment ratio process

Fixed	Output
$P_E = P_E^{rev}$	RER
$T_E = T_E^{rev}$	T_D^{rev}
$P_M = P_M^{rev}$	
$T_M = T_M^{rev}$	
$P_D = P_D^{rev}$	

[1]Where one is dealing with an ejector involving fluids of identical chemical composition, it is equivalent to define either the discharge pressure or the saturation temperature at that pressure, as is done by Al Khalidy and Zayonia [27] and by Elrod [19].

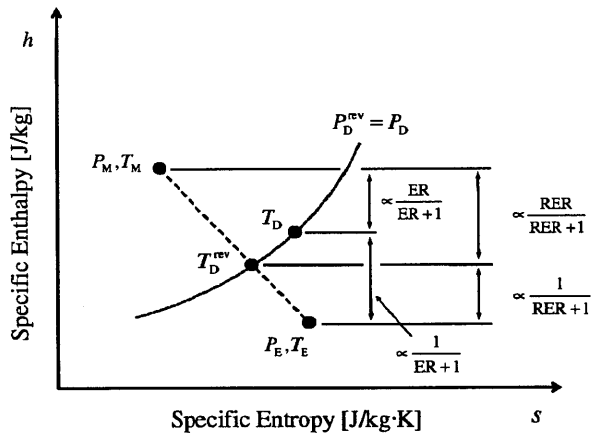

Figure 3-5: Graphical representation of the reversible entrainment ratio reference process

On an $h - s$ diagram, the reversible entrainment ratio reference process may be represented as:

The real discharge pressure in Fig. 3-5 is the same as that in Fig. 3-4. However, the discharge state is different. In the reversible entrainment ratio reference process, the reversible and real discharge pressure are set as equal. Employing the reversible entrainment ratio reference process, one may compare the real entrainment ratio to the entrainment ratio achieved in a reversible process.

Summary and Further Reference Processes

The above two reference processes are only two of the 21 possible reference processes for a dual inlet, pure and identical fluid ejector. In particular, knowledge of the entrainment ratio is interesting from a cost perspective as it quantifies the mass of fluid entrained per unit mass of motive fluid supplied. The reversible discharge pressure reference process is also considered due to the notable work presented on this process by Arbel *et al.* [22]. One could also consider a reference process whereby the motive and discharge state are fixed along with the entrainment ratio, and the

real entrained pressure and temperature are compared to the entrained pressure and temperature obtained in a reversible process. Having established a basis for the definition of such processes, further permutations are left to the reader bearing in mind that the choice of reference process must be guided by the intended application of the ejector.

3.2.3 Interpretation of a Thermodynamically Reversible Ejector Process

Here a thermodynamically reversible ejector process is further elucidated. Importantly, this illustration does not attempt to explain how a reversible process could be achieved in a real steady-flow ejector. Rather, it points out how, theoretically, a reversible process could take place within the control volume of an ejector. For simplicity, let us consider an ejector process with pure fluids at the inlet, both of identical chemical composition. The a reversible ejector process can now be interpreted as the sum of two processes. The first process establishes mechanical equilibrium and the second establishes thermal equilibrium. The process that establishes mechanical equilibrium at the discharge pressure, P_{D} is in fact a turbine-compressor processs. The motive and entrained fluids are respectively expanded and compressed through an adiabatic and isentropic turbine and compressor, Fig. 3-6.

The thermal equilibrating process may be represented by a reversible heat engine that transfers heat (and entropy) from the the hotter of the fluids M' or E' to the colder fluid, allowing them to reach an equilibrium temperature T_{D}. Of course, work is produced by the heat engine to supply the compression process. It is therefore clear, that in a reversible ejector process, the work available for compression is greater than that available in a turbine-compressor process. Consequently, the reversible entrainment ratio will always be greater than or equal to the turbine-compressor entrainment ratio. In the case where the fluid exiting the turbine and the compressor in Fig. 3-6 are at the same temperature, no work will be done by the reversible heat engine. Consequently, in this special case, the reversible entrainment ratio and the

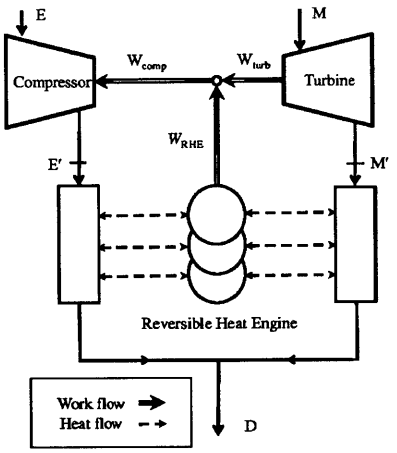

Figure 3-6: Schematic diagram of a thermodynamically reversible ejector for fluids of identical chemical composition

turbine-compressor entrainment ratio will be identical. The equilbrium process paths of Fig. 3-6 are represented in Fig. 3-7.

Until this stage, processes involving only pure and identical inlet fluids have been considered. However, the same analysis can be generalised to cover processes such as the compression of a moist air stream using high pressure steam. In such cases, additional variables, such as humidity ratio, are required to fully define the equilibrium state at any point.

3.3 Reversible Entrainment Ratio Calculations for Different Fluids

At present, the performance of ejectors is typically predicted using graphical methods or by semi-empirical correlations [28, 29]. These methods allow the calculation of the entrainment ratio as a function of inlet and outlet fluids' thermodynamic states. Whilst the reversible entrainment ratio does not provide much information about the entrainment ratio of real devices, it does provide an upper bound upon the entrain-

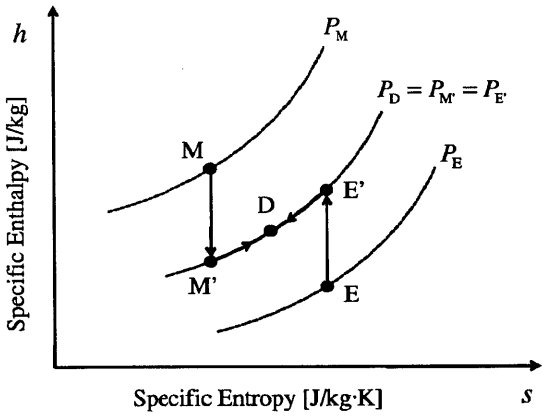

Figure 3-7: Process paths for a thermodynamically reversible ejector

ment ratio achievable. In this section, trends in the reversible entrainment ratio with inlet fluid conditions and discharge pressure are illustrated for ideal gases (air-air), steam-steam and steam-moist-carrier-gases ejectors.

3.3.1 Air-air

Derivation of the Reversible Entrainment Ratio for Ideal Gas Ejectors

For two reasons, the ideal gas ejector model is central to the understanding of ejector operation and performance characterization. First, the ideal gas assumptions allow analytical expressions to be derived for ejector performance. Secondly, for performance characterization of ejectors, the ideal gas model is appropriate for many ejector processes, as will be seen in Section 3.3.2.

Here an analytical expression is derived for the reversible entrainment ratio of an ideal gas process. The specific heat capacities of the gases at constant pressure are assumed to be equal and constant. The equation of state for an ideal gas is:

$$Pv = RT \tag{3.9}$$

where P is the total pressure, v the specific volume, R the ideal gas constant on a unit mass basis and T the total temperature. Equation (3.2) for ideal gases takes the following form for a reversible ejector process:

$$c_p T_{\mathrm{M}} + \mathrm{ER} \cdot c_p T_{\mathrm{E}} = (1 + \mathrm{ER}) c_p T_{\mathrm{D}} \tag{3.10}$$

Rearranging this equation, the discharge temperature may be written in terms of the inlet conditions and the reversible entrainment ratio:

$$T_{\mathrm{D}} = \frac{\mathrm{ER} \cdot T_{\mathrm{E}} + T_{\mathrm{M}}}{1 + \mathrm{ER}} \tag{3.11}$$

Rearranging Eq. (3.11) the following dimensionless equations are obtained:

$$\frac{T_{\mathrm{M}}}{T_{\mathrm{D}}} = \frac{1 + \mathrm{ER}}{1 + \mathrm{ER} \cdot \frac{T_{\mathrm{E}}}{T_{\mathrm{M}}}} \tag{3.12}$$

$$\frac{T_{\mathrm{D}}}{T_{\mathrm{E}}} = \frac{\frac{T_{\mathrm{M}}}{T_{\mathrm{E}}} + \mathrm{ER}}{1 + \mathrm{ER}} \tag{3.13}$$

Next, rearranging Eq. (3.7), the Second Law may be written as follows:

$$\mathrm{ER} = \frac{s_{\mathrm{M}} - s_{\mathrm{D}}^{\mathrm{rev}} + \frac{\dot{S}_{\mathrm{gen}}}{\dot{m}_{\mathrm{M}}}}{(s_{\mathrm{D}}^{\mathrm{rev}} - s_{\mathrm{E}})} \tag{3.14}$$

Here we seek an expression linking the change in entropy to the state properties T and P. The following expression describes a differential change in entropy of an ideal gas:

$$ds = c_p \frac{dT}{T} - \frac{v}{T} dP \tag{3.15}$$

$$ds = c_p \frac{dT}{T} - R \frac{dP}{P} \tag{3.16}$$

Now the entrainment ratio may be written as follows:

$$\mathrm{ER} = \frac{\frac{\dot{S}_{\mathrm{gen}}}{\dot{m}_{\mathrm{M}}} + \int_{\mathrm{D}}^{\mathrm{M}} c_p \frac{dT}{T} - \int_{\mathrm{D}}^{\mathrm{M}} R \frac{dP}{P}}{\int_{\mathrm{E}}^{\mathrm{D}} c_p \frac{dT}{T} - \int_{\mathrm{E}}^{\mathrm{D}} R \frac{dP}{P}} \tag{3.17}$$

For constant specific heats Eq. (3.17) results in the following relation describing the reversible entrainment ratio:

$$\mathrm{ER} = \frac{\frac{\dot{S}_{\mathrm{gen}}}{\dot{m}_{\mathrm{M}}} + c_p \ln(\frac{T_{\mathrm{M}}}{T_{\mathrm{D}}}) - R \ln(\frac{P_{\mathrm{M}}}{P_{\mathrm{D}}})}{c_p \ln(\frac{T_{\mathrm{D}}}{T_{\mathrm{E}}}) - R \ln(\frac{P_{\mathrm{D}}}{P_{\mathrm{E}}})} \tag{3.18}$$

Dividing the right hand side of Eq. (3.18) by the ideal gas constant, R, renders all terms dimensionless. Note also the definition, purely for convenience, of the dimensionless entropy generation rate.

$$\mathrm{ER} = \frac{\bar{s}_{\mathrm{gen}} + \frac{\gamma}{\gamma-1} \ln(\frac{T_{\mathrm{M}}}{T_{\mathrm{D}}}) - \ln(\frac{P_{\mathrm{M}}}{P_{\mathrm{D}}})}{\frac{\gamma}{\gamma-1} \ln(\frac{T_{\mathrm{D}}}{T_{\mathrm{E}}}) - \ln(\frac{P_{\mathrm{D}}}{P_{\mathrm{E}}})} \tag{3.19}$$

$$\bar{s}_{\mathrm{gen}} = \frac{\dot{S}_{\mathrm{gen}}}{\dot{m}_{\mathrm{M}} R} \tag{3.20}$$

Eq. (3.12), (3.13) and Eq. (3.19) allow the entrainment ratio to be expressed as a function of the following dimensionless parameters:

$$\mathrm{ER} = \mathrm{fn}(\mathrm{T_E/T_M}, \mathrm{P_E/P_M}, \mathrm{P_D/P_M}, \gamma, \bar{\mathrm{s}}_{\mathrm{gen}}) \tag{3.21}$$

The reversible entrainment ratio, RER, can now be defined in terms of the inlet fluid states and the discharge pressure using Eq. (3.19).

$$\mathrm{RER} = \frac{\frac{\gamma}{\gamma-1} \ln(\frac{T_{\mathrm{M}}}{T_{\mathrm{D}}}) - \ln(\frac{P_{\mathrm{M}}}{P_{\mathrm{D}}})}{\frac{\gamma}{\gamma-1} \ln(\frac{T_{\mathrm{D}}}{T_{\mathrm{E}}}) - \ln(\frac{P_{\mathrm{D}}}{P_{\mathrm{E}}})} \tag{3.22}$$

3.3.2 Steam-steam Reversible Entrainment Ratios

In this section, the reversible entrainment ratio is calculated for steam-steam ejectors. As a first step, let us ask how well steam-steam ejectors can be modelled using ideal

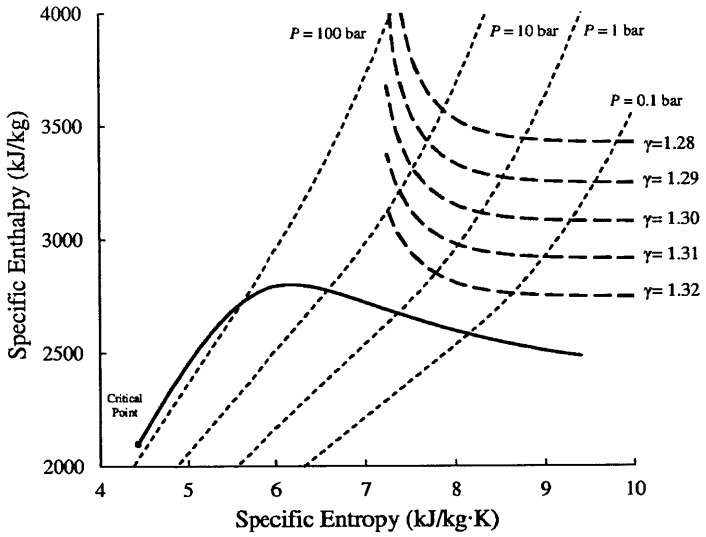

Figure 3-8: Lines of constant ratio of specific heats, γ, for steam

gas approximations. We note that steam-steam ejectors are typically supplied with supersaturated motive steam. This is done to avoid condensation within the ejector and a subsequent loss of mass via a condensate stream.

Steam behaves like an ideal gas at conditions of high temperature or low pressure. Supersaturated steam is very well approximated by ideal gas assumptions at pressures below approximately 10 bar. Above this pressure, ideal gas assumptions are only valid at higher levels of superheat. In Fig. 3-8, the saturation curve of pure water is plotted on axes of specific enthalpy versus specific entropy. The ratio of specific heats, γ, is calculated at a variety of points within the superheated region and plotted to demonstrate that γ is approximately constant in the low pressure superheated zone.

The entrained pressure and discharge pressure for steam ejectors are typically close to or below atmospheric pressure. Therefore, if the motive steam pressure is below about 10 bar, Eq. (3.12), (3.13) and (3.21) are approximately applicable in describing the inlet and outlet states of typical steam-steam ejectors.

The exact calculation of RER for steam is relatively straightforward. In each case the equations solved are Eq. (3.6) & (3.7). (If the state lies under the saturation curve, T and P would be insufficient to determine h and s. Instead, T and x, the

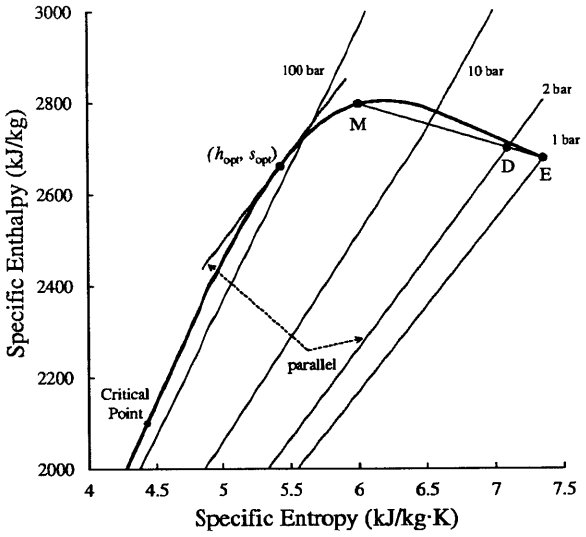

Figure 3-9: Specific enthalpy-entropy diagram for pure water

dryness fraction, or P and x would be required.) To graphically explain trends in the reversible entrainment ratio of a steam-steam ejector, Fig. 3-9 is provided. Figure 3-9 shows the states of the motive, discharge and entrained fluids on a specific enthalpy versus specific entropy diagram. The state of the discharge fluid is given by the intersection of the isobar at the discharge pressure and a line joining the motive and entrained states (again see Sect. 3.2 for derivation). The entrainment ratio is represented by the length of the line from the motive to the discharge state, |MD|, divided by the length of the line from the discharge to the entrained inlet state, |DE|, Eq. (3.23).

$$\text{RER} = \frac{|\text{MD}|}{|\text{DE}|} \tag{3.23}$$

For a fixed state of the entrained fluid, it may be shown that a motive saturated steam pressure exists that maximizes RER. In Fig. 3-10, RER is plotted as a function of the motive steam pressure, choosing inlet fluid dryness fractions of 100% for illustrative purposes. RER increases logarithmically until a motive steam pressure of approximately 15 bar is reached. Beyond a motive saturated steam pressure of 15

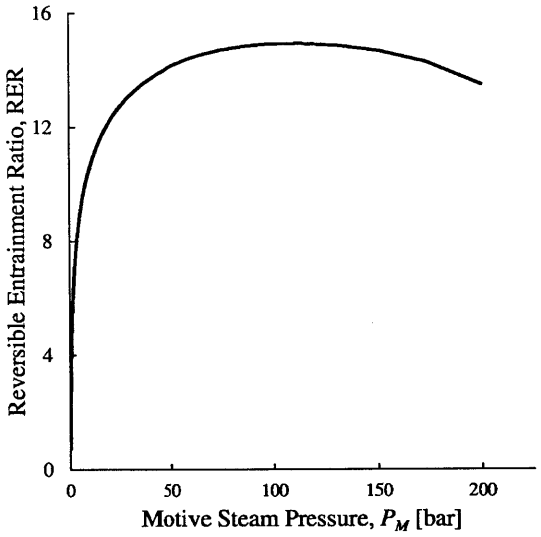

Figure 3-10: Reversible entrainment ratio versus motive steam pressure for a steam-steam ejector. (P_D=15 kPa, P_E=10 kPa, x_M=1, x_E=1)

bar, the rate of increase in RER reduces until an optimal motive steam pressure is reached. This optimum pressure corresponds to the point at which the tangent to the saturation curve is parallel to the slope of the isobar at the discharge state (see Fig. 3-9). This conclusion is reached by considering the point at which the distance |MD| divided by |DE| is maximised subject to point D lying at the intersection of the isobar at the discharge pressure and a line joining states M and E. The optimal pressure of the saturated motive fluid therefore depends upon the discharge pressure. As the discharge pressure changes, the slope of the isobar changes and thus the point at which the tangent to the saturation curve is tangential to the isobar at the discharge pressure also changes.

In Fig. 3-11, the optimal motive steam pressure is plotted for a fixed entrained fluid state and discharge pressure. The results are primarily of academic interest given that the optimal motive steam pressures are well beyond the typical pressures used in practical applications.

In Fig. 3-12 RER is plotted as a function of the discharge steam pressure. It is seen that RER drops drastically with an increasing compression ratio. Often, the

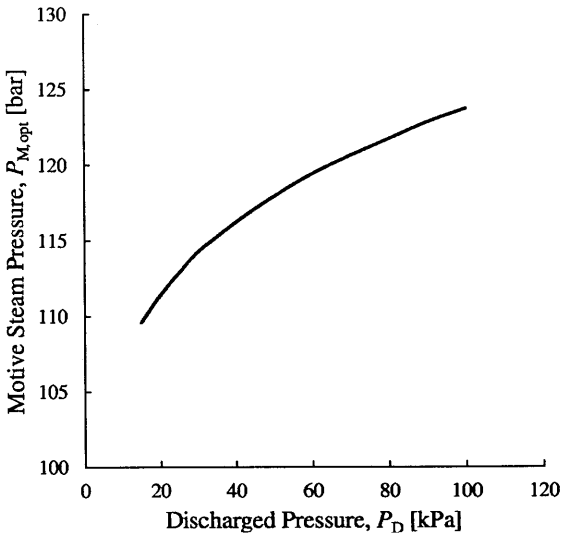

Figure 3-11: Optimal motive steam pressure of a steam-steam ejector

motive steam may be superheated and therefore it is interesting to consider the effect of the degree of superheating on RER. Figure 3-13 highlights the improvement in RER due to superheating at constant pressure of the motive steam.

In contrast to Fig. 3-10 and Fig. 3-12, the rate of change in RER is small with changes in the inlet motive steam temperature. Again, this trend may be visualised making use of Fig. 3-9. As the motive steam is superheated following an isobaric process, both its specific enthalpy and its specific entropy increase, although its specific enthalpy increases at a greater rate. This results in an increasing reversible entrainment ratio. The apparent linearity of Fig. 3-13 may be explained by the fact that the isobars in the superheated region of Fig. 3-9 are each approximately linear. Thus, the increase in reversible entrainment ratio, according to Eq. (3.23), will be linear.

Finally, we consider how RER can be maximized when there is an upper limit on the motive steam temperature. To do this we may plot RER at constant temperature against motive steam specific entropy, as is done in Fig. 3-14.

The line plotted in Fig. 3-14 is a line of constant temperature. The reversible entrainment ratio reaches a maximum when x=1, *i.e.* when the steam is in a saturated condition. Consider the entrainment of saturated steam at state E by saturated

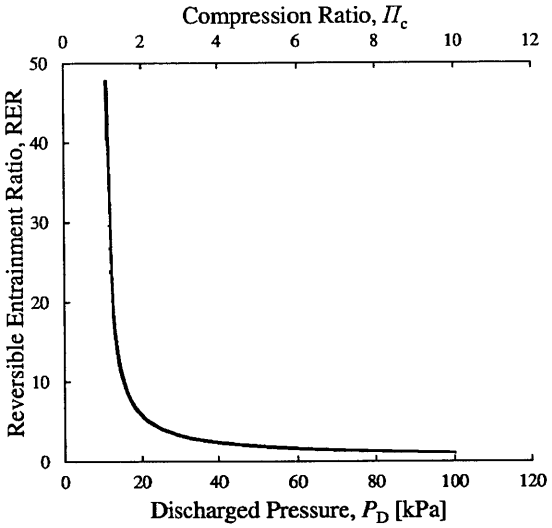

Figure 3-12: Reversible entrainment ratio versus discharge pressure for a steam-steam ejector. (P_M=10 bar, P_E=10 kPa, x_M=1, x_E=1)

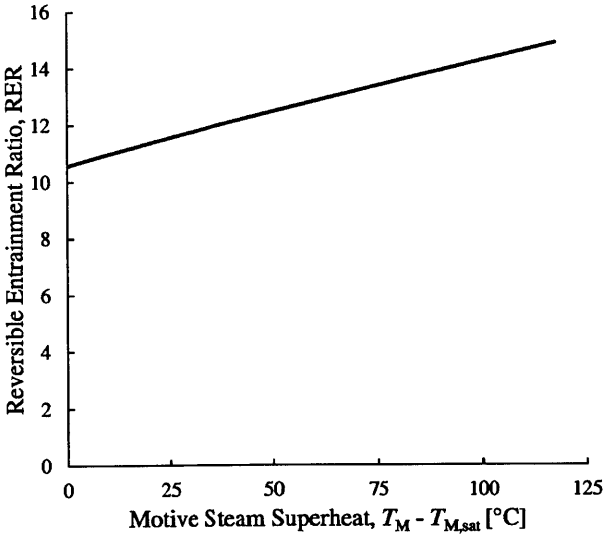

Figure 3-13: Reversible entrainment ratio versus motive steam superheat for a steam-steam ejector. (P_D=15 kPa, P_M=10 bar, P_E=10 kPa, x_E=1, $T_{M,sat}$ = 180 °C

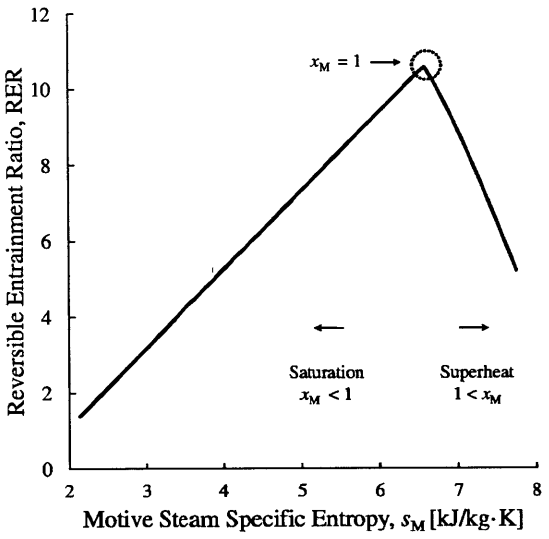

Figure 3-14: Reversible entrainment ratio versus motive steam specific entropy for a steam-steam ejector, with motive steam at constant temperature. (T_M=179.9 °C, $P_{sat,M}$=10 bar, P_D=15 kPa, P_E=10 kPa, x_E=1)

motive steam at state M (see Fig. 3-15). If the condition of the motive steam is brought below the saturation curve, the ratio of the line |MD| to |DE| decreases. Thus, because the isobars on a $h - s$ diagram of steam converge as the state moves from that of saturated steam to that of a wet mixture, RER using saturated motive steam will always be superior to that using a wet mixture at the same temperature. In the superheated region of the $h - s$ diagram, isobars and isotherms do not coincide. If state M moves along an isotherm into the superheated region, RER is severely compromised, as the isotherm corresponding to state M converges rapidly with and meets the isobar corresponding to the discharge state D. In real steam-steam ejectors, slightly superheated motive steam may preferentially be used to saturated steam in order to discourage the formation of droplets in the discharge, which may need to be removed using a mist eliminator.

As a final caveat, maximizing RER does not in any way maximize the exergetic efficiency of a real device. The RER represents a perfect and reversible process that is 100% efficient from a Second Law perspective. Rather, the purpose of this section

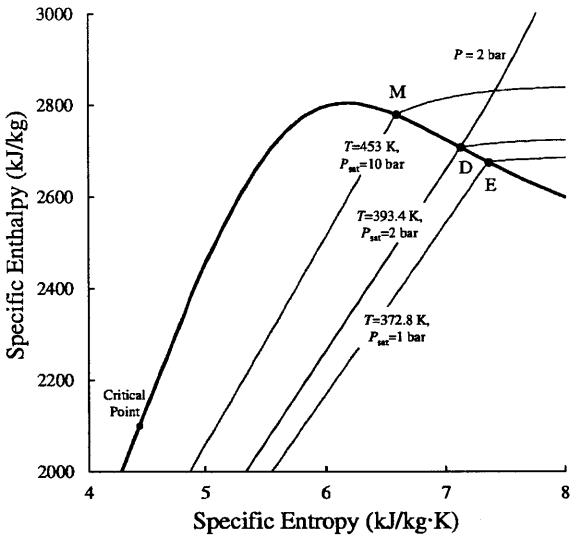

Figure 3-15: Isotherms on a specific enthalpy-entropy diagram for pure water

was to comprehend the upper thermodynamic limit on the entrainment ratio.

3.3.3 Steam-Moist-Gas Reversible Entrainment Ratios

Multipressure humidification-dehumidification (HDH) desalination cycles, which previously have been proposed by the current authors, make use of ejectors to pressurize a moist carrier gas [4, 5, 30]. It is therefore of interest to consider the effect upon the reversible entrainment ratio, RER, of using carrier gases of different types. In the case of a steam-moist-carrier-gas ejector, the entrainment ratio is defined as follows:

$$\mathrm{ER} = \frac{(1+\omega_{\mathrm{E}})\dot{m}_{\mathrm{cg}}}{\dot{m}_{\mathrm{M}}} \tag{3.24}$$

where ω_E is the humidity ratio of the entrained fluid. In the case of humidification-dehumidification desalination, the quantity of water vapor entrained is of importance, rather than the total amount of fluid entrained. For this reason, it is useful to define the vapor entrainment ratio. Of course, the vapor entrainment ratio is equivalent on a mass and molar basis as long as the motive fluid is steam.

$$\mathrm{ER}_{\mathrm{vap}} = \frac{\omega_{\mathrm{E}}\dot{m}_{\mathrm{cg}}}{\dot{m}_{\mathrm{M}}} = \mathrm{ER}\frac{\omega_{\mathrm{E}}}{1+\omega_{\mathrm{E}}} \tag{3.25}$$

In this section the entrained and discharge fluids are treated as ideal mixtures of ideal gases, within which the enthalpy and entropy of the carrier gas and steam are calculated at their partial pressures. The ratio of the number of moles of carrier gas and water vapor present in a moist carrier gas mixture along with the relative humidity are given as follows:

$$\xi = \frac{p_{\mathrm{vap}}}{P - p_{\mathrm{vap}}} = \frac{\dot{N}_{\mathrm{st}}}{\dot{N}_{\mathrm{cg}}} = \frac{\phi p_{\mathrm{sat}}}{P - \phi p_{\mathrm{sat}}} \tag{3.26}$$

When comparing the reversible entrainment ratio of different moist carrier gases, we do so at equal entrained fluid temperature, pressure and relative humidity. Therefore, it is sensible to consider the governing equations on a molar basis, since ξ is constant for all carrier gases under these conditions.

First Law of Thermodynamics (reversible process):

$$\dot{N}_{\mathrm{st,M}}\tilde{h}_{\mathrm{st,M}} + \dot{N}_{\mathrm{cg}}\tilde{h}_{\mathrm{cg,E}} + \dot{N}_{\mathrm{st,E}}\tilde{h}_{\mathrm{st,E}} = \dot{N}_{\mathrm{st,D}}\tilde{h}^{\mathrm{rev}}_{\mathrm{st,D}} + \dot{N}_{\mathrm{cg}}\tilde{h}^{\mathrm{rev}}_{\mathrm{cg,D}} \tag{3.27}$$

where $\dot{N}$ is a molar flow rate and $\tilde{h}$ is a molar enthalpy. According to a mole balance on steam:

$$\dot{N}_{\mathrm{st,D}} = \dot{N}_{\mathrm{st,M}} + \dot{N}_{\mathrm{st,E}} \tag{3.28}$$

$$\tilde{h}_{\mathrm{st,M}} + \frac{\mathrm{RER}_{\mathrm{vap}}}{\xi_{\mathrm{E}}}\tilde{h}_{\mathrm{cg,E}} + \mathrm{RER}_{\mathrm{vap}}\tilde{h}_{\mathrm{st,E}} = (1+\mathrm{RER}_{\mathrm{vap}})\tilde{h}^{\mathrm{rev}}_{\mathrm{st,D}} + \frac{\mathrm{ER}^{\mathrm{rev}}_{\mathrm{vap}}}{\xi_{\mathrm{E}}}\tilde{h}^{\mathrm{rev}}_{\mathrm{cg,D}} \tag{3.29}$$

Second law of Thermodynamics (reversible process):

$$\dot{N}_{\mathrm{st,M}}\tilde{s}_{\mathrm{st,M}} + \dot{N}_{\mathrm{cg}}\tilde{s}_{\mathrm{cg,E}} + \dot{N}_{\mathrm{st,E}}\tilde{s}_{\mathrm{st,E}} = \dot{N}_{\mathrm{st,D}}\tilde{s}^{\mathrm{rev}}_{\mathrm{st,D}} + \dot{N}_{\mathrm{cg}}\tilde{s}^{\mathrm{rev}}_{\mathrm{cg,D}} \tag{3.30}$$

$$\tilde{s}_{\mathrm{st,M}} + \frac{\mathrm{RER}_{\mathrm{vap}}}{\xi_{\mathrm{E}}}\tilde{s}_{\mathrm{cg,E}} + \mathrm{RER}_{\mathrm{vap}}\tilde{s}_{\mathrm{st,E}} = \tag{3.31}$$

$$(1 + \mathrm{RER}_{\mathrm{vap}})\tilde{s}^{\mathrm{rev}}_{\mathrm{st,D}} + \frac{\mathrm{RER}_{\mathrm{vap}}}{\xi_{\mathrm{E}}}\tilde{s}^{\mathrm{rev}}_{\mathrm{cg,D}} \tag{3.32}$$

Equations of State (reversible process):

$$\tilde{h}^{\mathrm{rev}}_{\mathrm{st,D}} = \mathrm{fn}(p^{\mathrm{rev}}_{\mathrm{st,D}}, \tilde{s}^{\mathrm{rev}}_{\mathrm{st,D}}) \tag{3.33}$$

$$\tilde{h}^{\mathrm{rev}}_{\mathrm{cg,D}} = \mathrm{fn}(p^{\mathrm{rev}}_{\mathrm{cg,D}}, \tilde{s}^{\mathrm{rev}}_{\mathrm{cg,D}}) \tag{3.34}$$

$\tilde{s}$ is the molar enthalpy. The partial pressures of the steam, $p_{\mathrm{st,D}}$, and carrier gas, $p_{\mathrm{cg,D}}$, both sum to the total discharge pressure, P_{D}. RER and $\mathrm{RER}_{\mathrm{vap}}$ are now plotted in Fig. 3-16 and Fig. 3-17 as a function of motive steam pressure, setting x_{M} and ϕ_{E} to unity for illustrative purposes.[2]

The results of Fig. 3-16 collapse onto a single curve in Fig. 3-17. Surprisingly, $\mathrm{RER}_{\mathrm{vap}}$ appears to be almost independent of carrier gas. Finally, in Fig. 3-18 the reversible vapor entrainment ratio is plotted versus the entrained fluid inlet temperature, maintaining a relative humidity of unity.

The increase in $\mathrm{RER}_{\mathrm{vap}}$ with temperature of the entrained moist carrier gas is explained by the decrease in value of the specific heat of the entrained fluid per mole of vapor.

3.4 Development of Ejector Performance Metrics

When one seeks to evaluate the thermodynamic ideality of a process, performance metrics are often chosen that compare useful work done in a real process to that in a defined reference process. However, the identification of work done within an ejector

[2]Note: Although not graphed here, the variation of reversible entrainment ratio with compression ratio for helium, air and carbon dioxide carrier gases is qualitatively similar to that obtained for steam-steam ejectors.

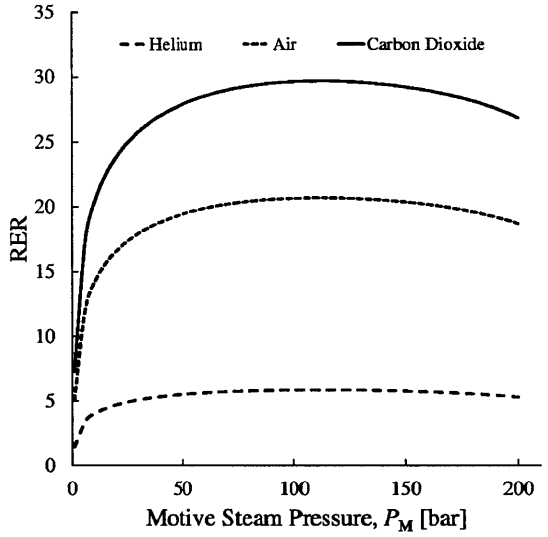

Figure 3-16: Reversible entrainment ratio versus motive steam pressure for steam-moist-carrier-gas ejectors. (P_D=75 kPa, P_E=50 kPa, T_E=50 °C, x_M=1, ϕ_E=1)

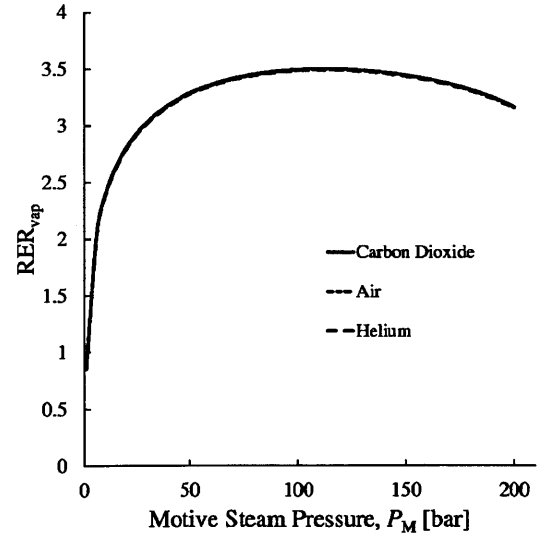

Figure 3-17: Reversible vapor entrainment ratio versus motive steam pressure for steam-moist-carrier-gas ejectors. (Π_c=1.5, P_E=50 kPa, T_E=50 °C, x_M=1, ϕ_E=1)

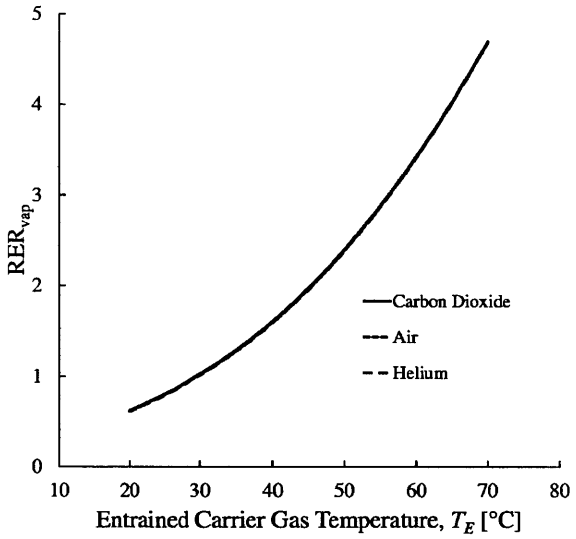

Figure 3-18: Reversible vapor entrainment ratio versus entrained saturated carrier gas temperature for a steam-moist-carrier-gas ejector. (P_{D}=75 kPa, P_{E}=50 kPa, Π_{i}=20, x_{M}=1, ϕ_{E}=1)

is not a trivial matter. In this section, these dilemmas are discussed and suggestions are made as to how performance metrics can be defined.

The crux of difficulties in evaluating work done within an ejector is that one cannot easily distinguish between useful flow work, heat transfer and dissipation. A similar difficulty is very clearly explained by Casey and Fesich [31] in relation to diabatic turbochargers, where heat transfer between the compressor and the turbine is significant. Maintaining the nomenclature of Casey and Fesich, the Gibbs equation may be integrated along the process path of a single fluid stream:

$$h_2 - h_1 = \int_1^2 v\,dp + \int_1^2 (T\,ds)_q + \int_1^2 (T\,ds)_{\mathrm{irrev}} = y_{12} + q_{12} + j_{12} \tag{3.35}$$

where y_{12} is the useful flow work done in the process, q_{12} is the reversible heat transfer and j_{12} is the dissipation, or in other words, the lost work. Whilst the change in enthalpy of the fluid is fixed by the end states, the useful flow work, the heat transferred and the dissipation are all path dependent. Only in the special case of an

adiabatic and reversible process can the useful flow work be equated with the change in enthalpy of the fluid:

$$h_2 - h_1 = \int_1^2 v\, dp \tag{3.36}$$

In reality, the motive and entrained streams in an ejector remain neither adiabatic nor distinct throughout the process. In real ejector processes, both heat transfer and dissipation are experienced by the motive and entrained streams during mixing. Consequently, the useful flow work can only be evaluated if the process path is known. Unfortunately, ejector mixing processes are characterized by a high degree of macroscopic disorder, involving heat transfer with finite temperature differences, forces that are not fully restrained and irreversible mixing. Intermediate states cannot accurately be represented on a process path of one intensive quantity against another. Consequently, there is no process path or equation in the form of Eq. (3.35) that can be applied to actual ejector processes.

Despite the difficulty of identifying useful work done in an ejector, there remain two broad approaches to characterising performance:

1. Comparisons may be made between terms representing useful work done in real and reference processes, provided that a clear rationale is given as to why such a metric compares different systems at different operating points. (Some performance metrics may only evaluate the performance of a part of the entire ejector process, as shall be seen with the turbine-compressor or compression efficiency.)

2. An exergy based approach may be taken. A performance metric may be defined once the useful exergetic output, the exergetic input, and a reference state for the process have been decided upon.

Next, four efficiencies based on the comparison of real and reversible processes are presented, followed by an exergetic efficiency.

3.4.1 Reversible Entrainment Ratio Efficiency

The definition of reversible entrainment ratio efficiency was provided in work by Elrod [19]. Al-Khalidy *et al.* [27] referenced the work of Elrod and also employed this efficiency. The reversible entrainment ratio efficiency η_{RER} quantifies how close the actual entrainment ratio of an ejector is to the theoretical maximum, for fixed conditions of operation. Its value is therefore always between zero and unity. RER is calculated based upon the reversible process described in Section 3.2.2.

$$\eta_{\mathrm{RER}} = \frac{\mathrm{ER}}{\mathrm{RER}} \tag{3.37}$$

For a process involving fluids with identical ratios of specific heats and behaving as ideal gases, the RER may be derived based upon the ideal gas analysis conducted in Section 3.3.1. The ratio of the real to reversible entrainment ratio may be written as follows:

$$\frac{\mathrm{ER}}{\mathrm{RER}} = \left(\frac{\bar{s}_{\mathrm{gen}} + \frac{\gamma}{\gamma-1}\ln(\frac{T_{\mathrm{M}}}{T_{\mathrm{D}}}) - \ln(\frac{P_{\mathrm{M}}}{P_{\mathrm{D}}})}{\frac{\gamma}{\gamma-1}\ln(\frac{T_{\mathrm{M}}}{T_{\mathrm{D}}}) - \ln(\frac{P_{\mathrm{M}}}{P_{\mathrm{D}}})} \right) \left(\frac{\frac{\gamma}{\gamma-1}\ln(\frac{T_{\mathrm{M}}}{T_{\mathrm{D}}}) - \ln(\frac{P_{\mathrm{M}}}{P_{\mathrm{D}}})}{\frac{\gamma}{\gamma-1}\ln(\frac{T_{\mathrm{M}}}{T_{\mathrm{D}}}) - \ln(\frac{P_{\mathrm{M}}}{P_{\mathrm{D}}})} \right) \tag{3.38}$$

One interesting case of ejector operation to consider is where the inlet temperatures of both ideal gases are equal. According to the First Law, the discharge temperature must equal the inlet temperatures in both real and reversible cases. Equation (3.22) then simplifies to a ratio of the natural logarithm of the expansion ratio $P_{\mathrm{M}}/P_{\mathrm{D}}$ to the ratio of the natural logarithm of the compression ratio $P_{\mathrm{D}}/P_{\mathrm{E}}$.

$$\mathrm{RER} = \frac{\ln(\frac{P_{\mathrm{M}}}{P_{\mathrm{D}}})}{\ln(\frac{P_{\mathrm{D}}}{P_{\mathrm{E}}})} \tag{3.39}$$

and the ratio of ER to RER simplifies to:

$$\frac{\mathrm{ER}}{\mathrm{RER}} = \frac{\ln(\frac{P_\mathrm{M}}{P_\mathrm{D}}) - \bar{s}_\mathrm{gen}}{\ln(\frac{P_\mathrm{M}}{P_\mathrm{D}})} \tag{3.40}$$

Finally, as a general comment, the principles of operation of steady flow ejectors impose further limits upon ejector performance that are not captured by a control volume analysis whereby the control volume surrounds the ejector. These internal limits depend both upon ejector geometry and operational conditions. Some of the most enlightening work in this regard has been conducted by Chou *et al.* [21] and Arbel *et al.* [22]. The same is true for the reversible discharge pressure efficiency, to be presented in the following section.

3.4.2 Reversible Discharge Pressure Efficiency

The reversible discharge pressure efficiency quantifies how close the actual rise in pressure of the entrained fluid is to the theoretical maximum pressure rise. As with the reversible entrainment ratio efficiency, it is bounded between zero and unity. The theoretical rise in pressure is calculated based upon Section 3.2.2. This efficiency is introduced and discussed in detail by Arbel et al [22].

$$\eta = \frac{P_\mathrm{D} - P_\mathrm{E}}{P_\mathrm{D}^\mathrm{rev} - P_\mathrm{E}} \tag{3.41}$$

3.4.3 Turbine-Compressor Efficiency

The turbine-compressor efficiency [1, 32–34] (also known as the turbomachinery analogue efficiency), allows the comparison of an ejector with a mechanically coupled turbine and compressor. The efficiency is defined as the ratio of the entrainment ratio in a real ejector to the entrainment ratio achieved in a turbo-charger exhausting to the same discharge pressure, P_D, as the ejector, and within which the turbine and compressor are adiabatic and isentropic (Fig. 3-19).

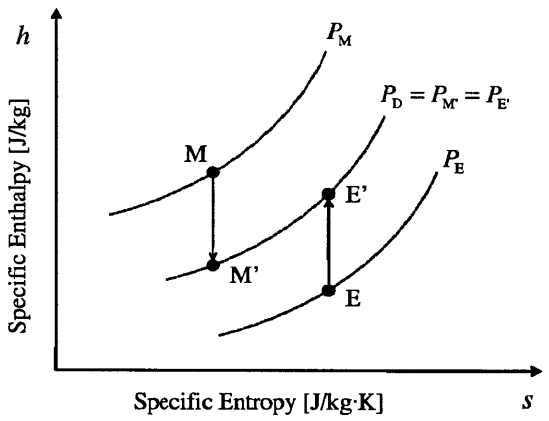

Figure 3-19: Isentropic expansion and compression processes

$$\eta_{\text{TER}} = \frac{\text{ER}}{\text{TER}} \tag{3.42}$$

Here, TER stands for Turbo Entrainment Ratio or Turbine-Compressor Entrainment Ratio. There is an important difference between the reversible entrainment ratio RER and the turbo entrainment ratio TER. The RER is calculated based on a process whereby the discharge is a single stream homogeneous in total temperature, total pressure and chemical composition. The TER is based upon a process whereby the inlet streams remain distinct at the discharge, *i.e.* the streams are not required to be in thermal or chemical equilibrium. Consequently, the value of TER will always be less than or equal to RER. A corollary of this is that η_{TER} is not bounded by an upper limit of 100%, as a real ejector could be imagined that achieves an entrainment ratio greater than that of a turbo, through the exploitation of the thermal or chemical disequilibrium of the fluids. Of course, a real steady-flow ejector could not in practice achieve a turbine-compressor entrainment efficiency beyond 100%. There is no obvious means by which a disequilibrium in chemical potential between the streams may be exploited. The question as to how thermal disequilibria may be exploited is more

complex. As shall be seen in Sect. 3.5, for ejectors designed to date, the difference in the value of η_{TER} and η_{RER} is small. Finally, η_{TER} may also be computed for a system comprising an independent turbine and compressor with the role of expanding one fluid and compressing a second, if the isentropic (also known as adiabatic) efficiencies of the turbine and compressor are known. Bulusu *et al.* [1] demonstrates the following equality:

$$\eta_{\mathrm{TER}} = \frac{\mathrm{ER}}{\mathrm{TER}} = \eta_{turb,s}\eta_{comp,s} \tag{3.43}$$

where $\eta_{turb,s}$ and $\eta_{comp,s}$ are the isentropic efficiencies of the turbine and compressor. Consequently, it may be said that an ejector with a turbine-compressor efficiency of 35% will provide the same performance as a turbine and compressor with isentropic efficiencies of 50% and 70% respectively, for example.

3.4.4 Compression Efficiency

Al-Najem *et al.* [23] presented the following measure of ejector performance, which here is denoted the compression efficiency:

$$\eta_c = \frac{(\dot{m}_{\mathrm{M}} + \dot{m}_{\mathrm{E}})\,(h_{\mathrm{D}} - h_{\mathrm{E}})}{\dot{m}_{\mathrm{M}}(h_{\mathrm{M}} - h_{M,\mathrm{NE}})} \tag{3.44}$$

where $h_{M,\mathrm{NE}}$ represents the static enthalpy at the exit of the motive fluid nozzle. Al-Najem *et al.* mention that this efficiency compares the compression work done in the ejector to the kinetic energy available from the motive stream. In a steady flow ejector, the nozzle through which the motive fluid is accelerated is adiabatic. The quantity $h_{\mathrm{M}} - h_{M,NE}$ represents the kinetic energy gained by the motive flow from the nozzle inlet to the exit. In an adiabatic mechanical compressor, the compression work done is given by $\dot{m}_{\mathrm{E}}(h_{\mathrm{D}} - h_{\mathrm{E}})$. Based upon this assertion, it seems likely that the quantity $h_{\mathrm{D}} - h_{\mathrm{E}}$ was selected to represent the compression work done in an ejector. However, in an ejector, heat transfer occurs between the motive and entrained streams during mixing. Therefore, the change in enthalpy $h_{\mathrm{D}} - h_{\mathrm{E}}$ is due to a combination of heating/cooling and work. Indeed, the useful compression work done in an ejector

requires the thermodynamic states describing the process path of the entrained fluid to be known. In conclusion, based upon the review of literature conducted, the rationale behind and the utility of the compression efficiency is unclear.

3.4.5 Exergetic Efficiency

Exergetic analysis is a means of evaluating ejector performance from a Second Law point of view. The premise of exergetic efficiency is to compare the useful exergetic output of a system or component to the exergetic input. First, for an exergetic efficiency to be meaningful, an environmental dead state must be defined. Let us consider an ejector operating within an environment at T_0 and P_0, as in Fig.3-2. $\dot{Q}_0$ represents the rate of heat input from the surroundings. For a steady-state process, the First and Second Laws take the following form:

$$(h_{\mathrm{M}} - h_{\mathrm{D,M}}) + \dot{Q}_0 = \mathrm{ER}\,(h_{\mathrm{D,E}} - h_{\mathrm{E}}) \tag{3.45}$$

$$(s_{\mathrm{M}} - s_{\mathrm{D,M}}) + \frac{\dot{Q}_0}{T_0} + \dot{S}_{\mathrm{gen}} = \mathrm{ER}\,(s_{\mathrm{D,E}} - s_{\mathrm{E}}) \tag{3.46}$$

where states D,M and D,E represent the state of the motive and entrained fluids in the discharge stream, calculated at their respective partial pressures. If the motive and entrained fluids do not differ in chemical composition, these states will be identical. Multiplying the Second Law by T_0 and subtracting the resulting equation from the First Law, the ejector process may be described in terms of flow exergy, x, a state variable.

$$(h_{\mathrm{M}} - h_{\mathrm{D}}) - T_0\,(s_{\mathrm{M}} - s_{\mathrm{D}}) = (h_{\mathrm{D}} - h_{\mathrm{E}}) - T_0\,(s_{\mathrm{D}} - s_{\mathrm{E}}) + T_0\dot{S}_{\mathrm{gen}} \tag{3.47}$$

$$-\Delta\dot{x}_{\mathrm{M}} = \mathrm{ER}\Delta\dot{x}_{\mathrm{E}} + T_0\dot{S}_{\mathrm{gen}} \tag{3.48}$$

$$\Delta\dot{x}_{\mathrm{E}} = (h_{\mathrm{D}} - h_{\mathrm{E}}) - T_0\,(s_{\mathrm{D}} - s_{\mathrm{E}}) \tag{3.49}$$

$$\Delta\dot{x}_{\mathrm{M}} = (h_{\mathrm{D}} - h_{\mathrm{M}}) - T_0\,(s_{\mathrm{D}} - s_{\mathrm{M}}) \tag{3.50}$$

The next step is to identify the exergetic output from and exergetic input to the system. This choice is somewhat subjective and depends on how the purpose of the ejector is defined. It may be argued that the role of an ejector is to transfer exergy from the motive fluid to the entrained fluid. This is somewhat analagous to a compressor or an extraction fan, where the device's role is to transfer exergy to a fluid. The value (or output) of the ejector process, in exergetic terms, may be measured by the change in exergy of the entrained fluid. The price paid to implement the process, again in exergetic terms, is the change in exergy of the motive fluid. Hence, the following formulation for exergetic efficiency, identical to that employed by Al-Najem *et al.* [23], is obtained:

$$\eta_X = \frac{\mathrm{ER}\Delta\dot{x}_\mathrm{E}}{-\Delta\dot{x}_\mathrm{M}} \tag{3.51}$$

Considering Eq. (3.47) it is clear that η_X also quantifies the exergetic losses per unit of exergetic input to the ejector process, Eq. (3.52).

$$1 - \eta_X = \frac{T_0\dot{S}_\mathrm{gen}}{\dot{m}_\mathrm{M}\left[(h_\mathrm{D} - h_\mathrm{M}) - T_0\left(s_\mathrm{D} - s_\mathrm{M}\right)\right]} \tag{3.52}$$

Comparison of the Exergetic and Reversible Entrainment Ejector Efficiencies

An analytical expression for the exergetic efficiency may be obtained when the inlet fluids are ideal gases of identical and constant specific heats. If the further restriction of having inlet fluids at the same temperature is imposed, the discharge enthalpy becomes independent of the entrainment ratio, Eq. (3.11). The discharge temperature equals the inlet temperature, and thus outlet and inlet specific enthalpies are also equal, Eq. (3.10). Consequently, the exergetic ejector efficiency takes the following form.

$$\eta_X = \mathrm{ER}\frac{(h_\mathrm{D} - T_0 s_\mathrm{D}) - (h_\mathrm{E} - T_0 s_\mathrm{E})}{(h_\mathrm{M} - T_0 s_\mathrm{M}) - (h_\mathrm{D} - T_0 s_\mathrm{D})} \tag{3.53}$$

$$= \mathrm{ER}\frac{-T_0 s_\mathrm{D} + T_0 s_\mathrm{E}}{-T_0 s_\mathrm{M} + T s_\mathrm{D}} \tag{3.54}$$

$$= \mathrm{ER}\frac{s_\mathrm{D} - s_\mathrm{E}}{s_\mathrm{M} - s_\mathrm{D}} \tag{3.55}$$

$$= \mathrm{ER}\frac{\ln\frac{P_\mathrm{D}}{P_\mathrm{E}}}{\ln\frac{P_\mathrm{M}}{P_\mathrm{D}}} \tag{3.56}$$

From Eq. (3.18), we an obtain the following expression for ER:

$$\mathrm{ER} = \frac{\ln(\frac{P_\mathrm{M}}{P_\mathrm{D}}) - \frac{\dot{S}_\mathrm{gen}}{R\dot{m}_\mathrm{M}}}{\ln(\frac{P_\mathrm{D}}{P_\mathrm{E}})} \tag{3.57}$$

Upon substituting Eq. (3.57) into Eq. (3.56), the exergetic ejector efficiency is found to be equal to the reversible entrainment ratio for an ideal gas ejector with identical specific heats and identical inlet temperatures:

$$\eta_X = \frac{\ln(\frac{P_\mathrm{M}}{P_\mathrm{D}}) - \frac{\dot{S}_\mathrm{gen}}{R\dot{m}_\mathrm{M}}}{\ln(\frac{P_\mathrm{M}}{P_\mathrm{D}})} = \eta_\mathrm{RER} \tag{3.58}$$

3.5 Comparison of Ejector Performance Metrics using Experimental Data

Now, having rigourously defined measures of ejector performance we may put these measures of efficiency to use in order to answer the following questions:

1. How do the numerical values of these efficiencies compare to one another?

2. What are the values of efficiency achieved by devices documented in literature?

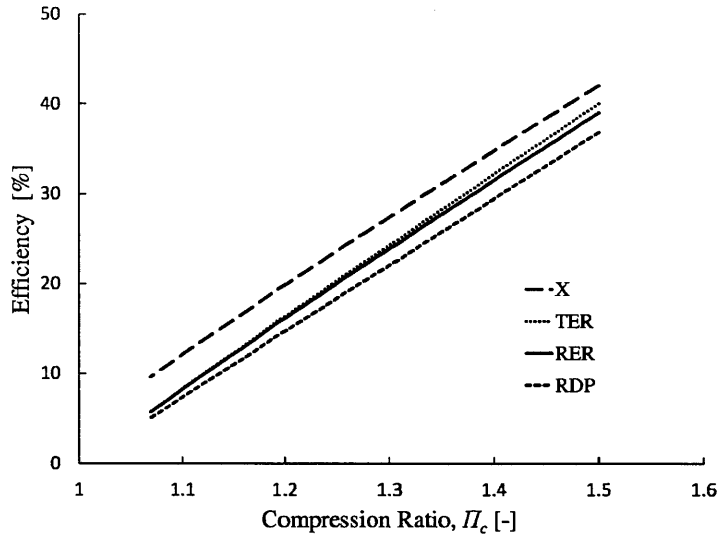

Figure 3-20: Comparison of efficiency definitions for a steam-steam ejector over a range of compression ratios

To answer the first question, we can simply compare a sample of fictitious ejector performance data. For example, we can compare the disparity in efficiency definitions over a range of compression ratios, P_D/P_E. Let us consider a single case involving the compression of saturated water vapor using high pressure saturated steam. Let us choose P_M=10 bar and P_E=50 kPa. Let us fix the performance of the real ejector by fixing ER (Note: we could also theoretically fix the real outlet state or the dimensionless entropy generation $\bar{s}_{gen}$). Now, in Fig. 3-20 the range of efficiencies are plotted versus the compression ratio, P_D/P_E. The compression efficiency is omitted due to its lack of rigour and its requirement for knowledge of a thermodynamic state internal to the ejector control volume.

To answer our second question, we must extract data from literature. One drawback of using such data is that the performance of ejectors analysed in literature is not necessarily representative of the state of the art ejectors employed in industry. Furthermore laboratory tests may not have been performed at the ejectors' design points of operation. With this caveat in mind, the efficiencies of an air-air and a steam-steam ejector are analysed, acknowledging that the conclusions drawn may

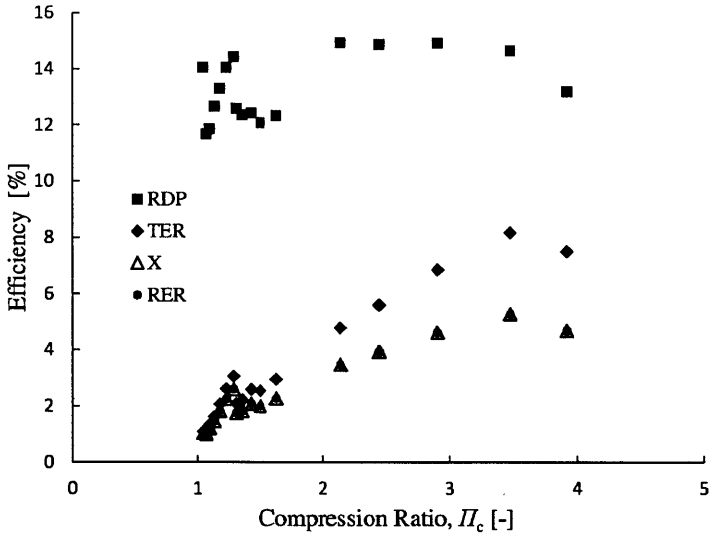

Figure 3-21: Comparison of efficiency definitions using data from an air-air ejector, [1, 2]. Chamber throat diameter, 0.88 inches; Diffuser exit diameter, 3.02 inches; Nozzle throat diameter, 0.5625 inches; Nozzle exit area 0.735 inches; Plenum diameter for secondary flow, 3.25 inches.

not be generalised to cover all ejectors. Amenable data for air-moist-carrier-gas ejectors was not available. Data for the air-air ejector was extracted from work by Bulusu *et al.* [1], Fig. 3-21. Data for the steam-steam ejector is from work by Eames *et al.* [3], Fig. 3-22. One should be aware that the degree of superheat of the motive steam is not obvious from the reported work and motive steam has been assumed to be saturated at the entrance to the ejector.

Note how, according to Eq. (3.58), the exergetic and reversible entrainment ratios are identical in value. The discrepancy in the turbine-compressor efficiency compared to the former two definitions is due to the fact that entropy generated in reaching thermal equilibrium of the fluids is unaccounted for.

Note that critical conditions of operation typically refer to the mode of ejector operation where the discharge pressure is such that choking of the entrained fluid occurs within the ejector. This choking is due to the formation of a hypothetical throat for the entrained fluid by the motive fluid expanding from the nozzle. For given inlet fluid conditions, the critical point of operation corresponds to the point

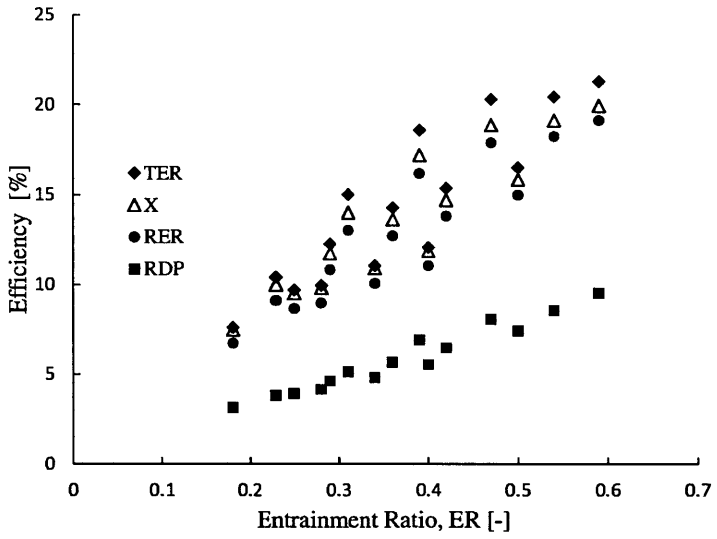

Figure 3-22: Comparison of efficiency definitions using data from a steam-steam ejector operating at conditions of critical back pressure [3]. Chamber throat diameter, 18 mm; Diffuser exit diameter, 40 mm; Nozzle throat diameter, 2 mm; Nozzle exit area 8 mm; Plenum diameter for secondary flow, 24 mm.

where the entrained mass flow rate is maximum. The occurance of choking within steady flow ejectors is dealt with in great detail by Chou *et al.* [21]. In Fig. 3-22 as in Fig. 3-21, the exergetic and reversible entrainment ratio efficiencies are similar in value although both demonstrate an increasing trend. The turbine-compressor efficiency is also close, and as expected, is greatest in value. Meanwhile the reversible discharge pressure efficiency differs significantly in value. This may be explained in two ways. Firstly, the reversible processes employed for the reversible discharge pressure and the reversible entrainment ratio are different. Secondly, the ratio of mass flows, employed in the reversible entrainment ratio, and the ratio of pressure rises of the entrained fluid, employed in the reversible discharge pressure clearly do not scale in the same manner.

3.6 Conclusions

In this chapter, various definitions of ejector efficiency have been evaluated. When defining or employing an ejector efficiency, it is crucial to describe the physical significance of the particular efficiency along with its utility. The following conclusions have been reached:

1. A reversible entrainment ratio may be calculated for any steady-flow ejector process, by employing the the First and Second Laws of thermodynamics, provided the thermodynamic states of the inlet fluids and the total pressure of the discharge fluid, all at equilibrium conditions, are known for a real ejector process.

2. The reversible entrainment ratio of an ideal gas ejector may be formulated analytically as a function of the inlet (motive-to-entrained) temperature and pressure ratios, the compression (discharge-to-entrained) pressure ratio and the ratio of specific heats. Calculation of the real entrainment ratio also requires knowledge of a further state variable describing the discharge (or alternatively the dimensionless entropy generation).

3. For steam-steam ejector applications, the inlet and outlet ejector states are shown to be accurately represented by ideal gas equations for pressures below 10 bar. Higher pressure motive steam may also be modelled as an ideal gas, provided the level of superheat is sufficient.

4. Where the motive fluid employed in a ejector is saturated steam, there exists an optimal pressure that maximizes the reversible entrainment ratio.

5. Where the temperature of motive steam is limited, the reversible entrainment ratio is maximized by employing saturated motive steam at a pressure equal to the saturation pressure at the maximum allowable temperature.

6. The reversible vapor entrainment ratio (ratio of vapor entrained to motive vapor) for steam-moist-carrier gas ejectors is insensitive to the choice of carrier

gas, if the inlet relative humidity is maintained constant.

7. The turbine-compressor entrainment ratio differs from the reversible entrainment ratio only in that the discharge fluids are unmixed and not brought into thermal and chemical equilibrium.

8. The reversible entrainment ratio RER is always greater than or equal to the turbine-compressor entrainment ratio TER.

9. The reversible entrainment ratio efficiency η_{RER} is always lower than the turbine-compressor efficiency η_{TER}.

10. For general air-air and steam-steam ejectors, the exergetic efficiency η_X is very close in numerical value to the reversible entrainment ratio efficiency η_{RER}.

11. The exergetic efficiency η_X for an ideal gas ejector with inlet fluids at the same temperature is identical to the reversible entrainment ratio efficiency η_{RER}.

12. The reversible entrainment ratio efficiency η_{RER} is advantageous compared to the exergetic efficiency η_X as its value does not depend upon the choice of a reference temperature.

Chapter 4

Recommendations

The research outlined in Chapter 2 leaves us with a clear idea of the limitations upon the performance of HDH systems, particularly where components of large size (small pinch point temperature and concentration differences) are concerned. However, a methodology for optimizing systems of fixed size is still required. The ejector research in Chapter 3 leaves us with a clear understanding of how the performance of different ejectors can be compared. In addition, we have a clear idea of how reversible ejectors would behave and can therefore quantify the limits upon real ejector performance. The next research step would be to investigate exactly why and when real ejector performance approaches reversibility and why and when this is not possible.

As is often the case, when we grow in understanding, opportunities to apply this understanding in the form of a new or improved technology arise. Here, two promising research ideas discovered during the course of my research, are outlined.

4.1 Reduced Temperature Range HDH Cycles

One of the key insights into the performance of HDH systems in Chapter 2 relates to our new understanding of the effect of temperature range upon performance. It was established that by reducing the temperature range of an HDH cycle, the GOR greatly improves whilst the recovery ratio decreases. One means of improving GOR would be to reduce the top temperature of the HDH cycle. Unfortunately, a lower temperature

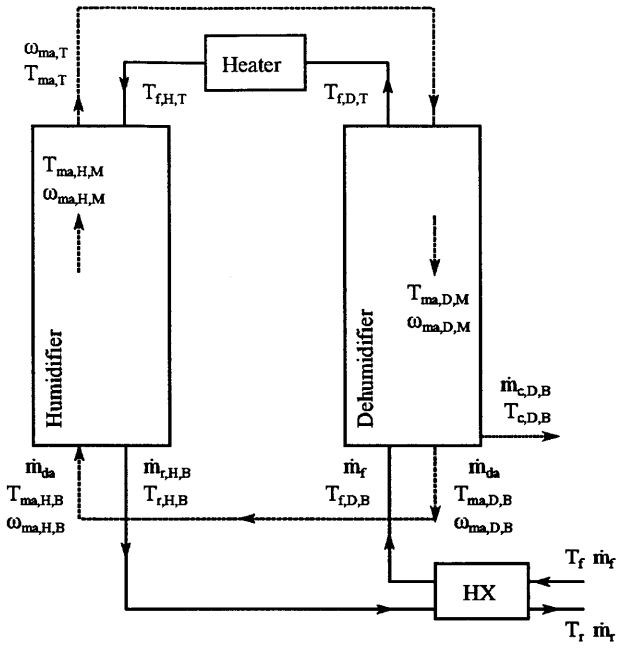

Figure 4-1: Low temperature range HDH configuration

HDH system operating at atmospheric pressure would also suffer from low fractions of vapor throughout, and conversely high carrier gas fractions. This higher fraction of carrier gases would lead to increased heat and mass transfer resistances, thus increasing the size and cost of the system.

Another, less obvious, solution is to increase the bottom temperature of the cycle. This may be done by employing a closed air cycle with a regenerating heat exchanger for the feed and reject streams, as in Fig. 4-1. Not only would the reduced temperature range improve the GOR, but the high fraction of vapor at higher temperatures would facilitate improved heat and mass transfer coefficients, leading to a smaller system size.

4.2 Future Research Directions

For heat and mass exchangers of finite size, the question remains as to what the optimal top and bottom temperatures would be. Furthermore, if the carrier gas is to operate in a closed loop, the choice of a carrier gas other than air may be advantageous,

particularly for reasons of improved thermal conductivity. Such questions would build upon the work of Narayan et al. [35].

4.3 Ejector-Expander Power Generation System

We now return to Fig. 1-1, where the combination of an ejector with an HDH system was presented in the introduction. This multi-pressure system was investigated in detail by Narayan et al. [5]. Due to the low amount of water produced in the dehumidifier of such a system relative to the power output of the expander, the system was found to be a power production cycle. Following this train of thought, and removing the humidifier from the system, the power production system of Fig. 4-2 is obtained.

Pure water flows in the upper loop and is pumped to high pressure, converted from the liquid to vapor phase in the heater, expanded within the ejector and then condensed in the dehumidifier. A carrier gas would flow in the lower loop, being compressed in the ejector, dehumidified and then expanded within the expander. The use of a bubbling column dehumidifier as investigated by Narayan et al. [36] may be ideal for such an application. Questions remain as to what the ideal pressures would be to achieve an optimal blend of efficiency and low capital cost. Furthermore, since the cycle operates with two closed loops, there is significant flexibility in the choice of fluids for both the upper and lower loops. The development of higher efficiency ejectors would also be a crucial step.

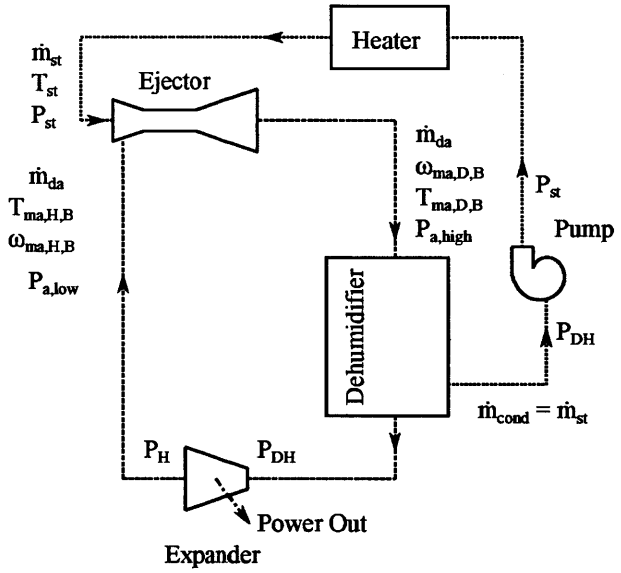

Figure 4-2: Ejector-expander shaft-power generation system

Bibliography

[1] K. V. Bulusu, D. M. Gould, C. A. Garris Jr., Evaluation of efficiency in compressible flow ejectors, in: 2008 ASME International Mechanical Engineering Congress and Exposition, IMECE 2008, October 31, 2008 - November 6, volume 8, American Society of Mechanical Engineers, Boston, MA, United States, 2008, pp. 531–554.

[2] K. V. Bulusu, Personal communication, 2011.

[3] I. Eames, S. Aphornratana, H. Haider, Theoretical and experimental study of a small-scale steam jet refrigerator, International Journal of Refrigeration 18 (1995) 378 – 386.

[4] G. P. Narayan, M. H. Sharqawy, J. H. Lienhard V, S. M. Zubair, Water separation under varied pressure, 2009. 2011/0079504 A1.

[5] G. P. Narayan, R. K. McGovern, S. M. Zubair, J. H. Lienhard V, High-temperature-steam-driven, varied-pressure, humidification-dehumidification system coupled with reverse osmosis for energy-efficient seawater desalination, Energy 37 (2012) 482–493. Accepted for publication in Energy.

[6] K. H. Mistry, R. K. McGovern, G. P. Thiel, E. K. Summers, S. M. Zubair, J. H. Lienhard V, Entropy generation analysis of desalination technologies, Entropy 13 (2011) 1829–1864.

[7] B. M. Hamieh, J. R. Beckman, Seawater desalination using dewvaporation technique: experimental and enhancement work with economic analysis, Desalination 195 (2006) 14 – 25.

[8] G. Narayan, M. Sharqawy, E. Summers, J. H. Lienhard, S. M. Zubair, M. Antar, The potential of solar-driven humidification-dehumidification desalination for small-scale decentralized water production, Renewable and Sustainable Energy Reviews 14 (2010) 1187–1201.

[9] S. Parekh, M. Farid, J. Selman, S. Al-Hallaj, Solar desalination with a humidification-dehumidification technique - a comprehensive technical review, Desalination 160 (2004) 167–186.

[10] G. P. Narayan, M. H. Sharqawy, J. H. Lienhard, V, S. M. Zubair, Thermodynamic analysis of humidification dehumidification desalination cycles, Desalination and Water Treatment 16 (2010) 339–353.

[11] S. Hou, S. Ye, H. Zhang, Performance optimization of solar humidification-dehumidification desalination process using Pinch technology, Desalination 183 (2005) 143–149. European Conference on Desalination and the Environment, St Margherita, ITALY, MAY 22-26, 2005.

[12] S. Hou, Two-stage solar multi-effect humidification dehumidification desalination process plotted from pinch analysis, Desalination 222 (2008) 572–578.

[13] M. Zamen, S. Soufari, M. Amidpour, Improvement of solar humidification-dehumidification desalination using multi-stage process, Chemical Engineering Transactions 25 (2011) 1091–1096.

[14] R. W. Hyland, A. Wexler, Formulations for the Thermodynamic Properties of the Saturated Phases of H_2O from 173.15 K to 473.15 K, ASHRAE Transactions 2A (1983).

[15] M. Sharqawy, J. H. Lienhard V, S. Zubair, Thermophysical properties of seawater: A review of existing correlations and data, Desalination and Water Treatment 16 (2010) 354–380.

[16] M. H. Sharqawy, J. H. Lienhard V, G. P. Narayan, S. M. Zubair, Water separation under reduced pressure, 2009.

[17] D. Tondeur, E. Kvaalen, Equipartition of entropy production. an optimality criterion for transfer and separation processes, Industrial & Engineering Chemistry Research 26 (1987) 50–56.

[18] G. P. Thiel, J. H. Lienhard V, Entropy generation in condensation in the presence of high concentrations of noncondensable gases (2011). Under Review.

[19] J. Elrod, H.G., The theory of ejectors, Journal of Applied Mechanics 12 (Sept. 1945) A170–A174.

[20] J. Keenan, E. Neumann, F. Lustwerk, Investigation of ejector design by analysis and experiment, American Society of Mechanical Engineers – Transactions – Journal of Applied Mechanics 17 (1950) 299 – 309.

[21] S. Chou, P. Yang, C. Yap, Maximum mass flow ratio due to secondary flow choking in an ejector refrigeration system, International Journal of Refrigeration 24 (2001) 486 – 499.

[22] A. Arbel, A. Shklyar, D. Hershgal, M. Barak, M. Sokolov, Ejector irreversibility characteristics, Transactions of the ASME. Journal of Fluids Engineering 125 (2003/01/) 121 – 9.

[23] N. Al-Najem, M. A. Darwish, F. A. Youssef, Thermovapor compression desalters: energy and availability - analysis of single- and multi-effect systems, Desalination 110 (1997) 223–238.

[24] O. A. Hamed, A. M. Zamamiri, S. Aly, N. Lior, Thermal performance and exergy analysis of a thermal vapor compression desalination system, Energy Conversion and Management 37 (1996) 379–387.

[25] A. O. B. Amer, Development and optimization of ME-TVC desalination system, Desalination 249 (2009) 1315–1331.

[26] F. N. Alasfour, M. A. Darwish, A. O. B. Amer, Thermal analysis of ME-TVC+MEE desalination systems, Desalination 174 (2005) 39–61.

[27] N. Al-Khalidy, A. Zayonia, Design and experimental investigation of an ejector in an air-conditioning and refrigeration system, in: Proceedings of the 1995 ASHRAE Annual Meeting, June 24, 1995 - June 28, volume 101, Silesian Technical Univ, Gliwice, Poland, ASHRAE, San Diego, CA, USA, 1995, pp. 383–391.

[28] H. El-Dessouky, H. Ettouney, I. Alatiqi, G. Al-Nuwaibit, Evaluation of steam jet ejectors, Chemical Engineering and Processing 41 (2002) 551–561.

[29] F. Al-Juwayhel, H. El-Dessouky, H. Ettouney, Analysis of single-effect evaporator desalination systems combined with vapor compression heat pumps, Desalination 114 (1997) 253 – 275.

[30] G. P. Narayan, K. H. Mistry, J. H. Lienhard V, S. M. Zubair, High efficiency thermal energy driven water purification system, 2011. USSN 13/028,170.

[31] M. V. Casey, T. M. Fesich, The efficiency of turbocharger compressors with diabatic flows, Journal of Engineering for Gas Turbines and Power 132 (2010) 072302.

[32] I. Watanabe, Experimental investigations concerning pneumatic ejectors, with special reference to the effect of dimensional parameters on performance characteristics, in: Jet pumps and ejectors; Proceedings of the Symposium, London, England; United Kingdom; 1 Nov. 1972, pp. 97–120.

[33] K. R. Hedges, P. G. Hill, Compressible flow ejectors. II. Flow field measurements and analysis, in: ASME-CSME Fluids Engineering Conference, volume 96, USA, pp. 282–8.

[34] K. Matsuo, K. Sasaguchi, Y. Kiyotoki, H. Mochizuki, Investigation of supersonic air ejectors - II. Effects of throat-area-ratio on ejector performance, Bulletin of the JSME 25 (1982) 1898–1905.

[35] G. P. Narayan, R. K. McGovern, S. M. Zubair, J. H. Lienhard V, Helium as carrier gas for humidification dehumidification desalination, in: 2011 International Mechanical Engineering Congress and Exhibition, IMECE 2011, November 11th - 17th, American Society of Mechanical Engineers, 2011.

[36] G. P. Narayan, G. P. Thiel, R. K. McGovern, M. H. Elsharqawy, J. H. Lienhard V, Multi-stage bubble column dehumidifier, 2011. USSN 13/241,907.